

# A Validated Mathematical Model of FGFR3-Mediated Tumor Growth Reveals Pathways to Harness the Benefits of Combination Targeted Therapy and Immunotherapy in Bladder Cancer

Kamaldeen Okuneye<sup>1</sup>, Daniel Bergman<sup>2</sup>, Jeffrey Bloodworth<sup>3</sup>, Alexander Pearson<sup>3</sup>, Randy Sweis<sup>3</sup>, and Trachette Jackson<sup>4</sup>

<sup>1</sup>Applied Biomath

<sup>2</sup>University of Michigan College of Literature Science and the Arts

<sup>3</sup>University of Chicago

<sup>4</sup>University of Michigan

January 30, 2024

## Abstract

Bladder cancer is a common malignancy with over 80,000 estimated new cases and nearly 18,000 deaths per year in the United States alone. Therapeutic options for metastatic bladder cancer had not evolved much for nearly four decades, until recently, when five immune checkpoint inhibitors were approved by the FDA. Despite the activity of these drugs in some patients, the objective response rate for each is less than 25%. At the same time, fibroblast growth factor receptors (FGFRs) have been attractive drug targets for a variety of cancers, and in 2019 the FDA approved the first therapy targeted against FGFR3 for bladder cancer. Given the excitement around these new receptor tyrosine kinase and immune checkpoint targeted strategies, and the challenges they each may face on their own, emerging data suggest that combining these treatment options could lead to improved therapeutic outcomes. In this paper, we develop a mathematical model for FGFR3-mediated tumor growth and use it to investigate the impact of the combined administration of a small molecule inhibitor of FGFR3 and a monoclonal antibody against the PD-1/PD-L1 immune checkpoint. The model is carefully calibrated and validated with experimental data before survival benefits and dosing schedules are explored. Predictions of the model suggest that FGFR3 mutation reduces the effectiveness of anti-PD-L1 therapy, that there are regions of parameter space where each monotherapy can outperform the other, and that pretreatment with anti-PD-L1 therapy always results in greater tumor reduction even when anti-FGFR3 therapy is the more effective monotherapy.

# **A Validated Mathematical Model of FGFR3-Mediated Tumor Growth Reveals Pathways to Harness the Benefits of Combination Targeted Therapy and Immunotherapy in Bladder Cancer**

Kamaldeen Okuneye<sup>1</sup> Daniel Bergman<sup>2</sup> Jeffrey C. Bloodworth<sup>3</sup> Alexander T. Pearson<sup>4,\*</sup>  
Randy F. Sweis<sup>3,\*</sup> Trachette L. Jackson<sup>2,\*</sup>

<sup>1</sup> Applied BioMath, LLC, Concord, Massachusetts, USA; kokuneye@appliedbiomath.com

<sup>2</sup> Department of Mathematics, University of Michigan, Ann Arbor, MI 48109, USA;  
bergmand@umich.edu

<sup>3</sup> Department of Medicine, Section of Hematology/Oncology, The University of Chicago, 5841 S  
Maryland Ave, MC 2115, Chicago, IL 60605 USA; rsweis@medicine.bsd.uchicago.edu

<sup>4</sup> Department of Medicine, Section of Hematology/Oncology, The University of Chicago, Chicago,  
IL 60637, USA; apearson5@medicine.bsd.uchicago.edu

\* Correspondence: tjacks@umich.edu, rsweis@medicine.bsd.uchicago.edu, and  
apearson5@medicine.bsd.uchicago.edu

## **Running Title:**

Modeling FGFR3-Targeted and anti-PD-L1 Therapy

## **Keywords:**

mathematical model, FGFR3-targeted therapy, immune checkpoint inhibitors, bladder cancer

## **Acknowledgments:**

This work was supported by NIH/NCI U01CA243075 (ATP, RFS, TLJ).

Submitted: December 30th, 2020

## 1 Abstract

2 Bladder cancer is a common malignancy with over 80,000 estimated new cases and nearly 18,000  
3 deaths per year in the United States alone. Therapeutic options for metastatic bladder cancer had  
4 not evolved much for nearly four decades, until recently, when five immune checkpoint inhibitors  
5 were approved by the FDA. Despite the activity of these drugs in some patients, the objective  
6 response rate for each is less than 25%. At the same time, fibroblast growth factor receptors  
7 (FGFRs) have been attractive drug targets for a variety of cancers, and in 2019 the FDA approved  
8 the first therapy targeted against FGFR3 for bladder cancer. Given the excitement around these  
9 new receptor tyrosine kinase and immune checkpoint targeted strategies, and the challenges they  
10 each may face on their own, emerging data suggest that combining these treatment options could  
11 lead to improved therapeutic outcomes. In this paper, we develop a mathematical model for FGFR3-  
12 mediated tumor growth and use it to investigate the impact of the combined administration of a  
13 small molecule inhibitor of FGFR3 and a monoclonal antibody against the PD-1/PD-L1 immune  
14 checkpoint. The model is carefully calibrated and validated with experimental data before survival  
15 benefits and dosing schedules are explored. Predictions of the model suggest that FGFR3 mutation  
16 reduces the effectiveness of anti-PD-L1 therapy, that there are regions of parameter space where  
17 each monotherapy can outperform the other, and that pretreatment with anti-PD-L1 therapy always  
18 results in greater tumor reduction even when anti-FGFR3 therapy is the more effective monotherapy.

## 19 1 Introduction

20 Bladder cancer is one of the 10 most common cancers in the United States and in advanced stages  
21 5-year survival rates are low (below 35%) [1]. For more than 30 years, therapeutic strategies  
22 have focused on the use of systemic chemotherapy before, during, or after loco-regional therapy  
23 [2]. Unfortunately, outcomes with chemotherapy are poor in advanced cases [3]. For this reason,  
24 researchers have turned their attention to targeted therapies.

25 Members of the fibroblast growth factor receptor (FGFR) family have become a successful  
26 therapeutic focal point for bladder cancer [4]. Genomic analysis of bladder cancer has identified

27 frequent alterations of FGFRs, including over-expression and mutations of FGFR3 that activate  
28 the receptor via ligand-independent dimerization [4]. Under normal conditions, heparin bound  
29 fibroblast growth factor (FGF) mediates FGFR3 dimerization, leading to kinase activation and  
30 stimulation of the extracellular-signal-regulated kinase (ERK) and protein kinase B (AKT) signaling  
31 pathways, followed by increased cell proliferation and cell survival [4]. FGFR3 mutations that lead  
32 to constitutive activation of downstream signaling pathways in the absence of FGF are commonly  
33 found in bladder cancers. Urothelial bladder carcinoma has the most established association with  
34 altered FGFR3 signaling, with up to 80% of low-grade tumors harboring FGFR3 mutations [5].  
35 Clinical trials using small molecule inhibitors (SMIs) of FGFR3 show promising clinical responses  
36 for patients with FGFR3 mutations and in 2019, the FDA approved the first therapy targeted  
37 against FGFR3 [4].

38 At the same time, immunotherapy has now emerged as an exciting domain for exploration for  
39 many cancers including bladder cancer. The recent success of programmed cell death protein 1  
40 (PD-1) and programmed death-ligand 1 (PD-L1) blockade in cancer therapy illustrates the impor-  
41 tant role of the PD-1/PD-L1 checkpoint in the regulation of anti-tumor immune responses [6]. In  
42 particular, monoclonal antibodies (mAbs) targeting the PD-1/PD-L1 pathway have resulted in fa-  
43 vorable outcomes in advanced bladder cancer and 6 immune checkpoint inhibitors (ICIs) targeting  
44 this pathway were approved in 2015-2018 [7]. Despite therapeutic potential of ICIs, only a minority  
45 (approximately 20%) of bladder cancer patients respond favorably to these therapies and median  
46 survival with second line immunotherapy remains shorter than 1 year [8]. Figure 1 is a schematic  
47 diagram showing the impact of FGFR3 mutations and PD-1-PD-L1 checkpoints on tumor growth  
48 and tumor cell - T cell interactions.

49 Given the potential and challenges ICIs on their own, it is possible that the co-acting combina-  
50 tion of potent immune checkpoint inhibitors and specific FGFR3 inhibitors can offer much-needed  
51 improvements in targeted therapeutics for bladder cancer. The the rationale for combining FGFR3-  
52 targeted therapy with immunotherapy is confirmed in preclinical and correlative literature and  
53 animal models suggest potential synergies between these two mechanisms [8]. When attempting to  
54 combine two very different therapeutic approaches that target distinct pathways, treatment out-

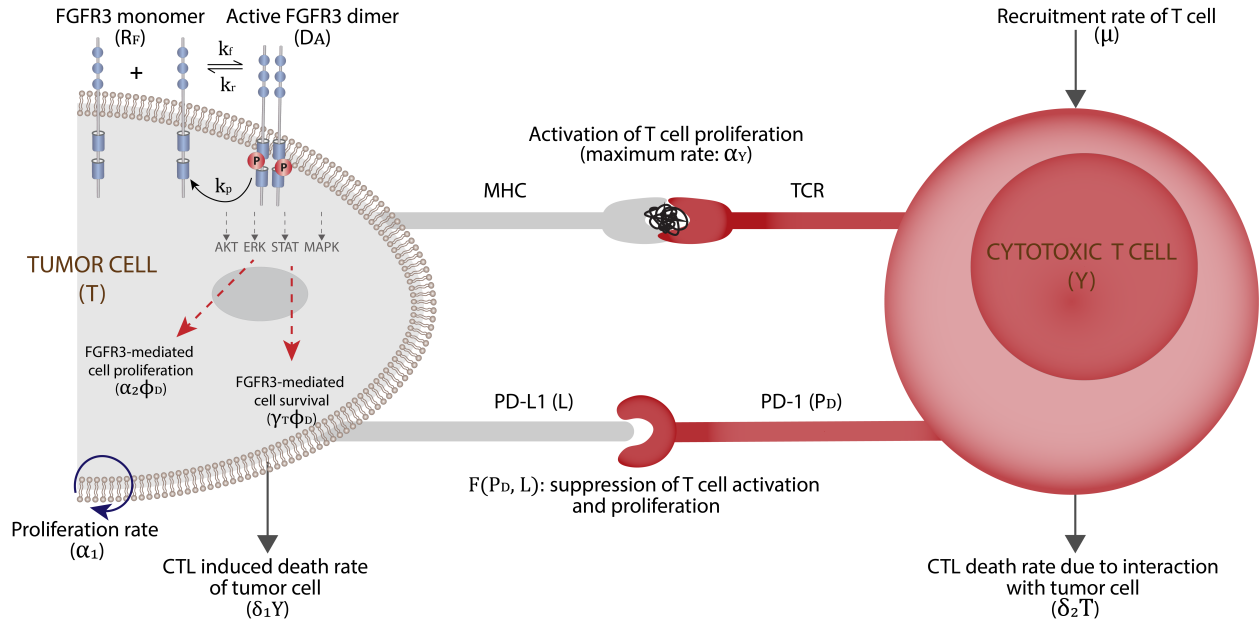


FIGURE 1. Microenvironment of tumor cell showing the dynamics of FGFR3 mutation on tumor cells (phosphorylation of the kinase region leads activation of AKT, ERK, STAT, and MAPK proteins which result into target DNA transcription leading to cell proliferation and cell survival), the activation of T cell by tumor cells, and suppression of T cell activation and proliferation by PD-L1 binding with PD-1.

55 comes can depend on the order and timing in which therapies are administered. Experimental  
 56 studies of the most appropriate strategy for FGFR3 inhibition in the context of ICI therapy (either  
 57 through sequencing or combination) are generally in early clinical stages. Data driven mathematical  
 58 modeling is an ideal tool for analyzing novel drug combinations for clinical cancer treatment and  
 59 here we design a model to investigate FGFR3 mediated tumor growth and response to combination  
 60 targeted and ICI therapy. The sections below describe the details of model development, sensitivity  
 61 and identifiability analysis, parameter estimation, and therapeutic predictions.

## 62 2 Model Formulation

63 Our mathematical model is based on the current biological understanding of bladder cancer growth  
 64 when the FGFR3 mutation is present. We first develop a pretreatment model that describes the  
 65 impact of ligand-independent activation of FGFR3 on tumor growth and CTL mediated death.  
 66 Next, we extend the pretreatment model to include anti-PD-L1 therapy alone and in combination

with FGFR3-targeted therapy. These models are used to predict the impact of therapy on survival outcomes and to suggest the best dose scheduling regimes for therapeutic efficacy.

## 2.1 Model Formulation with FGFR3 and Immune Checkpoints

The pretreatment model, described in detail below, captures the local evolution of free FGFR3 ( $R$ ) and active FGFR3 dimer complexes ( $D$ ) on tumor cells ( $T$ ) as well as PD-1 ( $P_D$ ) and PD-L1 ( $L$ ) mediated immune cell ( $Y$ ) kill. The model variables and their units are described in Table 1.

TABLE 1. Description of Variables

Variable	Description	Units
$R$	Free FGFR3 monomer receptors	nmol
$D$	Active FGFR3 dimer complexes	nmol
$T$	Tumor cells	cells
$Y$	Cytotoxic T cells (CTL)	cells
$P_D$	PD-1	nM
$L$	PD-L1	nM

The equations in (1) below describe the ligand-independent dimerization of FGFR3. Parameters that mediate these FGFR3 dynamics include the receptor association rate ( $k_f$ ) and dissociation rate ( $k_r$ ). It is also known that activated receptors undergo stimulated endocytosis but can continue to signal along the endocytic pathway [9] so we also include terms for receptor internalization and recycling rate ( $k_p$ ). For a full list of parameters see Table 2.

$$\begin{aligned}
 \frac{dR}{dt} &= -2k_f R^2 + 2k_r D + 2k_p D + R_T \mathcal{P}(T, \phi_D) - \frac{R}{R + 2D} R_T \mathcal{D}(T, Y, \phi_D) \\
 \frac{dD}{dt} &= k_f R^2 - k_r D - k_p D - \frac{D}{R + 2D} R_T \mathcal{D}(T, Y, \phi_D)
 \end{aligned}
 \tag{1}$$

These ODEs must account for changes in receptor number due to cellular proliferation and apoptosis. The last two terms in the equation for free receptors ( $R$ ) describes the generation of new receptors as cells divide and the loss of receptors as cells die, respectively, where  $R_T$  is the total number of FGFR3 molecules on tumor cells and  $\frac{R}{R+2D}$  is the fraction of free FGFR3 that is removed from the loss of tumor cells ( $T$ ) by cytotoxic T cells ( $Y$ ). The FGFR-dependent proliferation growth and death rates of tumor cells (i.e.,  $\mathcal{P}(T, \phi_D)$  and  $\mathcal{D}(T, Y, \phi_D)$ ) are defined in the temporal dynamics of

84 the tumor cells described below, where  $\phi_D$  is the fractional occupancy of active FGFR3 dimer per  
 85 cell defined by:

$$\phi_D = \frac{1}{R_T} \frac{D}{T}. \quad (2)$$

86 Equation (3) below models the temporal dynamics of the tumor cells

$$\frac{dT}{dt} = (\alpha_1 + \alpha_2 \phi_D)T - \frac{\delta_1 Y}{1 + \gamma_T \phi_D} T \equiv \mathcal{P}(T, \phi_D) - \mathcal{D}(T, Y, \phi_D) \quad (3)$$

87 The first term in Equation (3) describes tumor cells with high antigenicity proliferating exponentially  
 88 with a natural growth rate  $\alpha_1$ , and an FGFR-mediated tumor growth rate  $\alpha_2$ . The second term in  
 89 Equation (3) describes the killing of tumor cells by cytotoxic T cells ( $Y$ ) modified by the impact of  
 90 FGFR3 on tumor survival, where  $\delta_1$  is the death rate of a tumor cell by cytotoxic T cells, and  $\gamma_T$  is  
 91 the sensitivity of fractional occupancy of FGFR. This formulation assumes that the total number  
 92 (converted to nmol using molecular weight) of receptors per tumor cell  $R_T$  remains constant. This  
 93 means that the total amount of FGFR3 in the system should be conserved. We can ensure that the  
 94 model equations do conserve FGFR3 by considering the sum of the equations of the model (1):

$$\frac{dR}{dt} + 2 \frac{dD}{dt} = R_T [\mathcal{P}(T, \phi_D) - \mathcal{D}(T, Y, \phi_D)] = R_T \frac{dT}{dt},$$

95 Therefore, upon integration, we have

$$R + 2D = R_T T.$$

96 The equation for the change in cytotoxic T cells ( $Y$ ) is given by:

$$\frac{dY}{dt} = \left( \mu + \alpha_Y \frac{T}{\kappa + T} Y \right) F(P_D, L) - \delta_2 T Y - \delta_Y Y \quad (4)$$

97 The first term in Equation (4) represents a constant recruitment/activation of T cells at a rate,  $\mu$ .  
 98 The second term describes proliferation that occurs as the result of antigenic stimulation by the  
 99 tumor cells. The maximum proliferation rate is  $\alpha_Y$  and  $\kappa$  represents the population of  $T$  at which the

100 immune cells lyse tumor cells at half of their maximum killing rate [10]. The factor  $F(P_D, L)$ , which  
 101 is described in greater detail below, represents the suppression of T cell activation and proliferation  
 102 via the PD-1/PD-L1 checkpoint. The variables  $P_D$  and  $L$  denote the molar concentrations of PD-1  
 103 and PD-L1, respectively, expressed by cells within the model. The molar concentrations are obtained  
 104 by first calculating the PD-1 expression on all T cells and the PD-L1 expression on all T cells and  
 105 tumor cells as outlined in the Appendix found in [10]. Our formulation of  $F(P_D, L)$  in Equation  
 106 (7) below ensures that as  $P_D$  and  $L$  increases so does the number of PD-1/PD-L1 complexes within  
 107 the tumor region. This increase corresponds to a smaller  $F(P_D, L)$  value, modeling the inhibition  
 108 of T cell activity. Finally, the last two terms describe how CTLs can die. Specifically, interaction  
 109 with tumor cells can result in death at a rate  $\delta_2$  as was done in [11], but which sets our model apart  
 110 from [10, 12, 13]. CTLs can also die naturally at a rate  $\delta_Y$ .

111 We assume that all T cells express PD-1 and that the temporal dynamics of this cell-bound  
 112 protein is proportional to the rate of change of the T cells on which they reside as described by  
 113 Equation 5. This is the same approach used in [10, 12, 13].

$$\frac{dP_D}{dt} = \rho_P \frac{dY}{dt} \quad \Rightarrow \quad P_D = \rho_P Y \quad (5)$$

114 where,  $\rho_P$  is the cell rate of expression of PD-1 on T cells. Again, following [10, 12, 13], the molar  
 115 concentration of PD-L1 ( $L$ ) within the tumor micro-environment is given by

$$L = \rho_L(Y + \epsilon T) \quad (6)$$

116 where  $\rho_L$  is the is the molar concentration of PD-1 per T cell and the parameter  $\epsilon > 1$  reflects the  
 117 fact that the expression of PD-L1 is upregulated on tumor cells (and depends on the specific type of  
 118 tumor). Finally, we choose the following functional form for T cell suppression via PD-1 signaling,  
 119  $F(P_D, L)$ , just as in [10, 12, 13] by

$$F(P_D, L) = \frac{1}{1 + P_D L / K_{YQ}}. \quad (7)$$

120 The parameter values and their sources for the full pretreatment model are provided in Table 2.

TABLE 2. Pretreatment Parameter Values

Variable	Description	Range of value (Baseline)	Units	Source
FGFR3-related				
$k_f$	FGFR3 association rate	$1 - 5 \times 10^{11}$ ( $4.16 \times 10^{11}$ )	$\text{nmol}^{-1} \text{d}^{-1}$	[14]
$k_r$	FGFR3 dissociation rate	$10 - 2000$ (864)	$\text{d}^{-1}$	[14]
$k_p$	FGFR3 recycling rate	$10 - 150$ (112.32)	$\text{d}^{-1}$	[14]
$R_T$	Total FGFR3 receptors	$1.49 - 1.74 \times 10^{-11}$ ( $1.66 \times 10^{-11}$ )	$\text{nmol cell}^{-1}$	[15]
Tumor-related				
$\alpha_1$	Proliferation rate	$0.12 - 0.51$ (0.337)	$\text{d}^{-1}$	Best fit
$\alpha_2$	FGFR3-mediated proliferation rate	$0.001 - 0.1$ (0.00774)	$\text{d}^{-1}$	Best fit
$\delta_1$	CLT-mediated death rate	$1 - 2.5 \times 10^{-7}$ ( $1.1 \times 10^{-7}$ )	$\text{cell}^{-1} \text{d}^{-1}$	[11]
$\gamma_T$	FGFR3-enhanced survival sensitivity	$0.1 - 0.5$ (0.3018)		Best fit
T cell-related				
$\mu$	Activation/recruitment rate	$1 - 2 \times 10^4$ ( $1.3 \times 10^4$ )	$\text{cell d}^{-1}$	[11]
$\alpha_Y$	Max proliferation rate	$0.1 - 0.5$ (0.3044)	$\text{d}^{-1}$	[11, 12, 16]
$\kappa$	Proliferation half-saturation constant	$10^6 - 3 \times 10^7$ ( $2.019 \times 10^7$ )	cell	[11]
$\delta_2$	Tumor-mediated death rate	$2 - 4 \times 10^{-10}$ ( $3.422 \times 10^{-10}$ )	$\text{cell}^{-1} \text{d}^{-1}$	[11]
$\delta_Y$	Natural death rate	$0 - 0.05$ (0.0412)	$\text{d}^{-1}$	[10]
$\rho_P$	PD-1 per cell	$10^{-9} - 10^{-7}$ ( $1.258 \times 10^{-8}$ )	nM	[10]
$\rho_L$	PD-L1 per cell	$10^{-9} - 2 \times 10^{-7}$ ( $2.51 \times 10^{-8}$ )	nM	[10]
$\epsilon$	Tumor - immune PD-L1 ratio	$1 - 100$ (50)		[10, 12, 16]
$K_{YQ}$	Immune checkpoint inhibition constant	$10^{-4} - 10^{-2}$ ( $1.296 \times 10^{-3}$ )	$\text{nM}^2$	[10]

## 121 2.2 Model Formulation with FGFR3, Immune Checkpoints, and Combination 122 Therapy

123 In this section, we extend our pretreatment model equations to incorporate the therapeutic admin-  
124 istration of an immune checkpoint inhibitor (ICI) in the form of a monoclonal antibody against

125 PD-L1 and a small molecule inhibitor (SMI) targeting the FGFR3 pathway. We refer to the former  
 126 as anti-PD-L1 therapy and the latter as anti-FGFR3 therapy and our goal is to study the response  
 127 of tumor cells to these therapies alone and in combination. See Figure 2 for a schematic description  
 of a tumor cell undergoing anti-FGFR3 and anti-PD-L1 combination therapy.

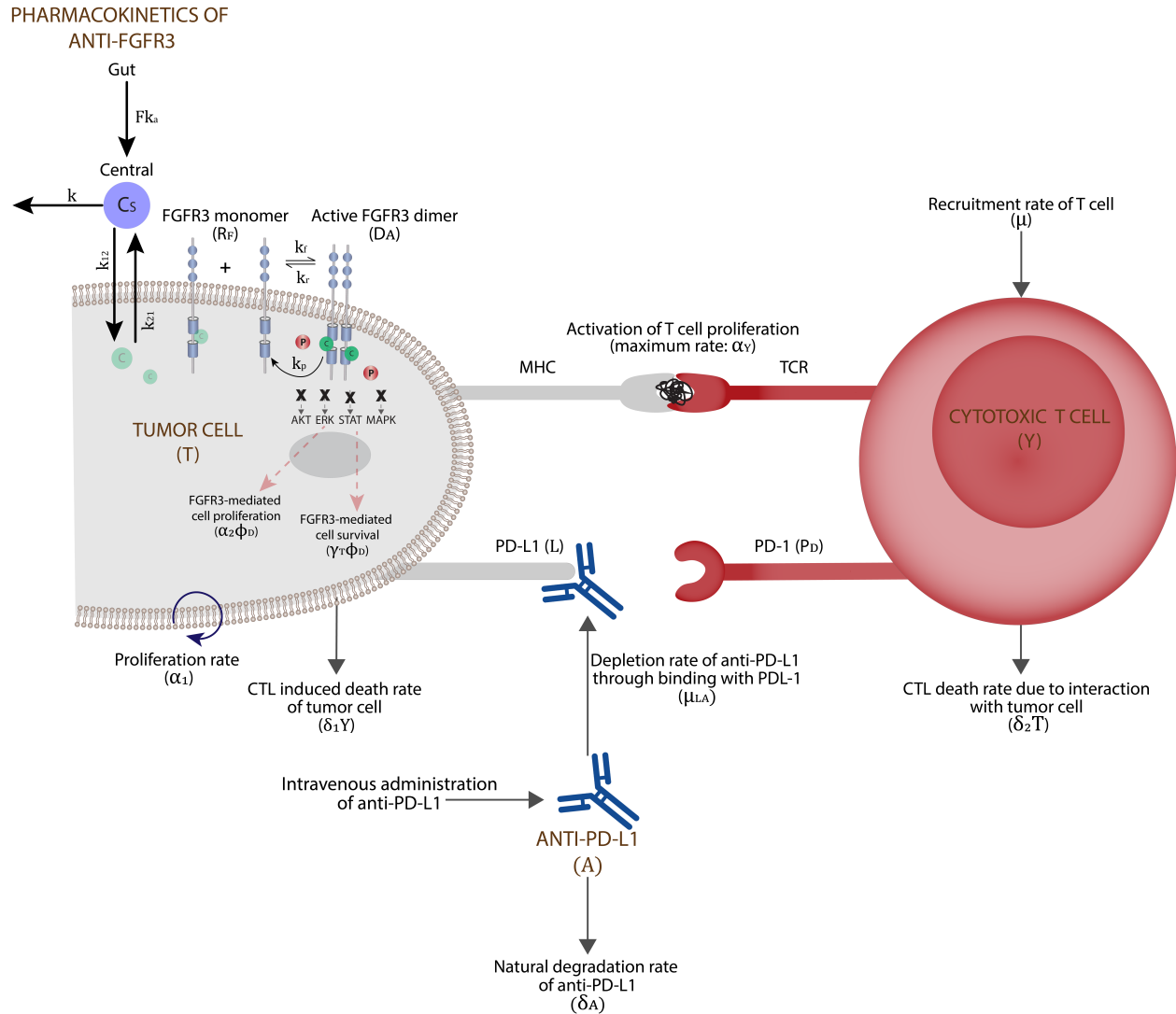


FIGURE 2. Microenvironment of tumor cell with combination therapy of anti-FGFR3 drug plus anti-PD-L1 antibody. We assume that anti-FGFR3 drug binds with both FGFR3 monomers and dimers. Anti-PD-L1 antibody targets PD-L1, thus inhibiting its binding with PD-1 and enabling T cell activation and proliferation.

128

129 An anti-PD-L1 antibody (A) binds to PD-L1 and inhibits the formation of the PD-1-PD-L1

130 complex. Following [10, 12, 13], the equation for the change in anti-PD-L1 antibody is given by:

$$\frac{dA}{dt} = -\mu_{LA}LA - \delta_A A, \quad (8)$$

131 with an initial condition,  $A(0)$ , that represents the amount of anti-PD-L1 antibody administered via  
 132 intraperitoneal injection at different time points,  $\mu_{LA}$  is the depletion rate of anti-PD-L1 antibody  
 133 through binding with PDL-1 ( $L$ ) and  $\delta_A$  is the natural degradation rate of anti-PD-L1 antibody.  
 134 Upon administration of an anti-PD-L1 antibody, the equation for the change in cytotoxic T cells  
 135 (given in Equation (4)) is modified and given by:

$$\frac{dY}{dt} = \left( \mu + \alpha_Y \frac{T}{\kappa + T} Y \right) F(P_D, L, A) - \delta_2 T Y - \delta_Y Y. \quad (9)$$

136 The functional form  $F(P, L, A)$  given by:

$$F(P_D, L) = \frac{1}{1 + \frac{P_D L}{K_{YQ}} \left( 1 - \frac{A}{A + K_D} \right)}. \quad (10)$$

137 where  $K_D$  is the dissociation constant of the PD-L1/anti-PD-L1 complex. The factor  $F(P_D, L, A)$   
 138 represents the impact of an anti-PD-L1 by reducing the number of PD-1/PD-L1 complexes within  
 139 the tumor region. In the absence of an anti-PD-L1 antibody (i.e.,  $A = 0$ ), the factor  $F(P_D, L, A)$   
 140 becomes  $F(P_D, L)$  given by Equation (7). See Appendix A for the full derivation of  $F(P_D, L, A)$ .

141 By binding to the kinase activity region of the receptors, an anti-FGFR3 drug (rogaratinib)  
 142 inhibits the phosphorylation of the FGFR3 kinase domain and the downstream signaling of AKT,  
 143 MAPK, ERK, and STAT [17, 18, 19]. To incorporate the therapeutic administration of rogaratinib,  
 144 we designed a pharmacokinetic model with oral administration of rogaratinib. We assume that the  
 145 tumor resides in a pharmacokinetic compartment of its own, and rogaratinib is transferred into the  
 146 tumor from the systemic circulation at the same rate as the peripheral tissue. The pharmacokinetics  
 147 of rogaratinib and the system of equations (and all the underlying assumptions) governing the  
 148 dynamics of FGFR3 in the tumor cell in the presence of rogaratinib are given in Appendices B and  
 149 C, respectively.

150 Overall, the temporal dynamics of the tumor cells in the presence of combination therapy of  
 151 anti-FGFR3 and anti-PD-L1 is given by:

$$\frac{dT}{dt} = (\alpha_1 + \alpha_2 \phi_D^C)T - \frac{\delta_1 Y}{1 + \gamma_T \phi_D^C} T \equiv \mathcal{P}(T, \phi_D^C) - \mathcal{D}(T, Y, \phi_D^C) \quad (11)$$

152 where  $\phi_D^C$  is the fractional occupancy of active FGFR3 dimer per cell in the presence of anti-FGFR3  
 153 drug (described in Appendix A) and the temporal dynamics of cytotoxic T cells ( $Y$ ) are given by  
 154 Equation (9).

### 155 3 Pretreatment Results

#### 156 3.1 Parameter Sensitivity

157 We use uncertainty and sensitivity analysis to determine the parameters that have the greatest  
 158 effect on tumor growth in the FGFR3 mutation model without treatments (Equations (1), (3),  
 159 and (4)). Global sensitivity analysis quantifies the impact of the variations or sensitivity of each  
 160 parameter of the model on the model outcomes [20, 21, 22]. In particular, following [21, 22], Latin  
 161 hypercube sampling (LHS), and the partial rank correlation coefficient (PRCC) will be used for  
 162 this analysis. The sensitivity analysis of the model is carried out using the tumor volume (in  
 163  $\text{mm}^3$ ) at the final time point, which is defined as  $\frac{T(t_f)}{10^6}$  where  $t_f = 25$  d. The range and baseline  
 164 values of the parameters, tabulated in Table 2, will be used. The result depicted in Figure 3 shows  
 165 that the parameters that significantly affect the tumor growth dynamics are the natural growth  
 166 rate of tumor cells ( $\alpha_1$ ), the CTL mediated death rate of tumor cells ( $\delta_1$ ), and FGFR3-mediated  
 167 tumor proliferation ( $\alpha_2$ ), and the sensitivity of tumor survival to FGFR3 ( $\gamma_T$ ). Overall, these  
 168 results indicate that therapies (monotherapies or combination therapies) that reduce the natural  
 169 growth rate of tumor cells, increase the death rate of tumor cells by cytotoxic T-cells (e.g. the use  
 170 of antibodies to target the immune checkpoint PD-1/PD-L1 pathway to active cytotoxic T-cells),  
 171 and/or decreasing fractional occupancy of FGFR3 dimer complexes on tumor cells (e.g., the use  
 172 of anti-FGFR3 drugs to target the FGFR3 pathway) will be effective in controlling and treating  
 173 bladder cancer with FGFR3 mutation.

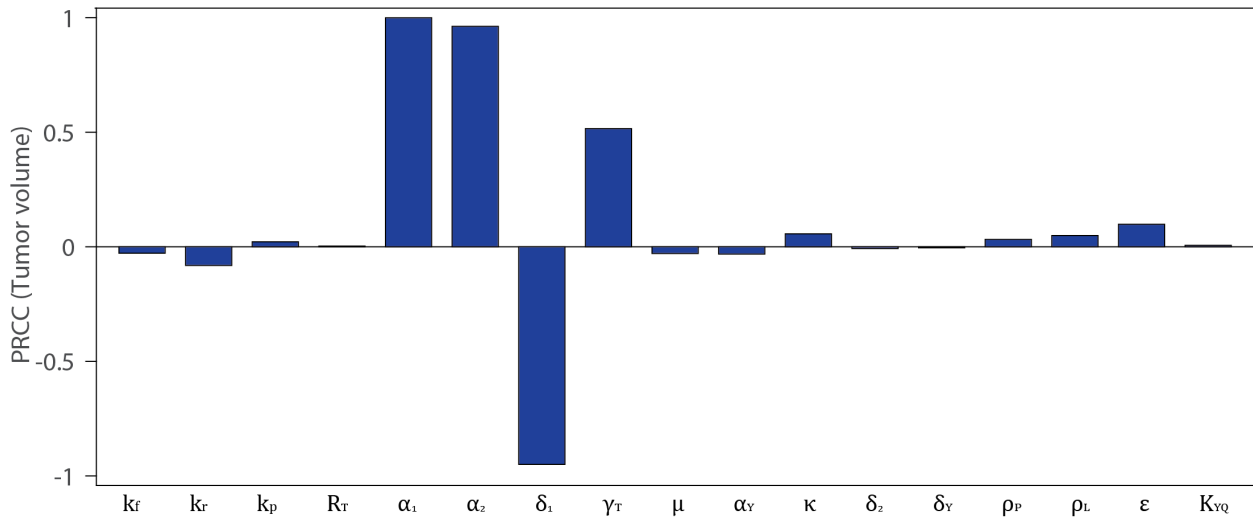


FIGURE 3. Sensitivity analysis of models (1), (3), and (4) showing PRCC values for the model parameters using the tumor volume as a response function. The baseline and range of parameter values used are given in Table 2.

174

## 175 3.2 Pretreatment Identifiability

176 To determine which model parameters, if any, can be uniquely estimated from a given data set  
 177 (and to what degree of certainty), we employ identifiability analysis [23]. This toolkit allows us to  
 178 determine the subset(s) of identifiable parameters and explore their interplay without even using  
 179 experimental data for parameter estimation and model calibration [24]. We examine both structural  
 180 and practical identifiability of the model parameters.

### 181 3.2.1 Structural Identifiability

182 First, we perform a structural identifiability analysis to determine whether or not it is possible to  
 183 obtain a unique solution for the parameters while assuming perfect data (noise-free and continuous  
 184 in time and space) [25, 26, 27, 28]. Specifically, we consider the subset of the sensitive parameters  
 185 identified in Section 3.1 and determine if they can be uniquely estimated from measurements of  
 186 values of all the model variables (active dimer complexes on tumor cells, tumor volume, and the  
 187 number of cytotoxic T cells). The structural identifiability of the model is analyzed using the

188 MATLAB package GenSSI (see [25, 28] for complete details).

189 We obtained an identifiability tableau in Figure 4A that shows 8 non-zero rows—indicated by  
190 black regions and corresponding to non-zero generating series coefficients—that depend on the sen-  
191 sitive parameters. If any parameters from the identifiability tableau can be computed as functions  
192 of the power series coefficients and eliminated, then a reduced tableau is obtained [25], as shown in  
193 Figure 4B. Using the GenSSI algorithm, we obtained unique solutions for all the sensitive paramete-  
194 ters  $(\alpha_1, \delta_1, \alpha_2, \gamma_T)$ , that is, they are globally identifiable. Thus, the model is globally structurally  
195 identifiable, which indicates that error-free time series data of all the model variables would be  
196 sufficient to identify a unique subset of the four parameters.

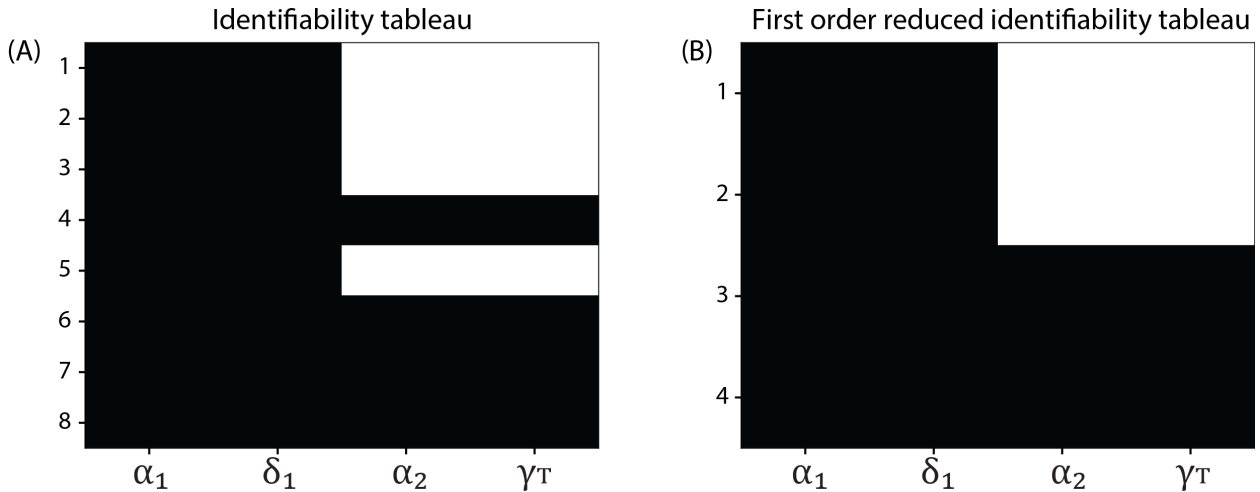


FIGURE 4. Model identifiability results with the subset of four most sensitive parameters the model. (A) Identifiability tableau. (B) Results and reduced tableau. All four parameters shown are globally identifiable.

### 197 3.2.2 Practical Identifiability

198 In practice, complete time-series and noiseless experimental data for structural identifiability are  
199 not available. Therefore, in this section, we carry out a practical identifiability analysis to deter-  
200 mine whether the most-sensitive parameters are identifiable from noisy experimental data of tumor  
201 volume. To do this, we seek to determine whether a distribution with a clear mode can be deter-  
202 mined for each of the sensitive parameters given such data. We used the Markov chain Monte Carlo

203 (MCMC) method with Metropolis-Hastings sampling [25]. Given simulated data for the system  
204 output, prior distributions of the parameter values, and a likelihood function, the MCMC samples  
205 the posterior distributions of the parameter, and the Metropolis-Hastings updating scheme accepts  
206 the new sample with probability given by the ratio of the new likelihood to the old likelihood [25].

207 Specifically, we use uniform distributions as prior distributions on the parameters within the  
208 ranges given in Table 2. To create the likelihood functions, we use the experimental data for  
209 tumor volume without FGFR3 mutation – to determine the practical identifiability of  $\alpha_1$  and  $\delta_1$  –  
210 and the experimental data for tumor volume with FGFR3 mutation – to determine the practical  
211 identifiability of  $\alpha_2$  and  $\gamma_T$ . The tumor volume for each day is assumed to be log-normally distributed  
212 about the mean tumor volume at each time point and truncated to be within one standard deviation  
213 of this mean. The joint probability distribution of these is then used to create the likelihood  
214 functions for the two applications of the MCMC method. We first used MCMC to estimate the  
215 posterior distributions for  $\alpha_1$  and  $\delta_1$  and then separately used it for  $\alpha_2$  and  $\gamma_T$ . In both cases, we  
216 used a chain length of 10,000 to sample from the posterior distributions.

217 The result depicted in Figure 5A in the form of one-dimensional histograms and two-dimensional  
218 heat maps shows that  $\alpha_1$  has a normal distribution and  $\delta_1$  has a broad distribution within its range  
219 in Table 2, thus indicating that  $\alpha_1$  is practically identifiable and  $\delta_1$  is not practically identifiable.  
220 Then, by sampling from this posterior distribution and forward simulating, we generate model  
221 predictions of tumor volume distributions without FGFR3 mutation at the sample time points  
222 that are tightly controlled and match the corresponding distributions from the data (Figure 5B).  
223 Similarly, using experimental data for mean tumor volume with FGFR3 mutation, our simulation  
224 showed that  $\alpha_2$  and  $\gamma_T$  have a normal and a broad distribution, respectively (Figure 5C), within  
225 its range in Table 2. Hence,  $\alpha_2$  is practically identifiable, and  $\gamma_T$  is not practically identifiable  
226 given the available experimental data. We again sample from the posterior distribution and forward  
227 simulate to generate tumor volume distributions with FGFR3 mutation, and again we see that these  
228 distributions are tightly controlled and match the corresponding data distribution (Figure 5D).

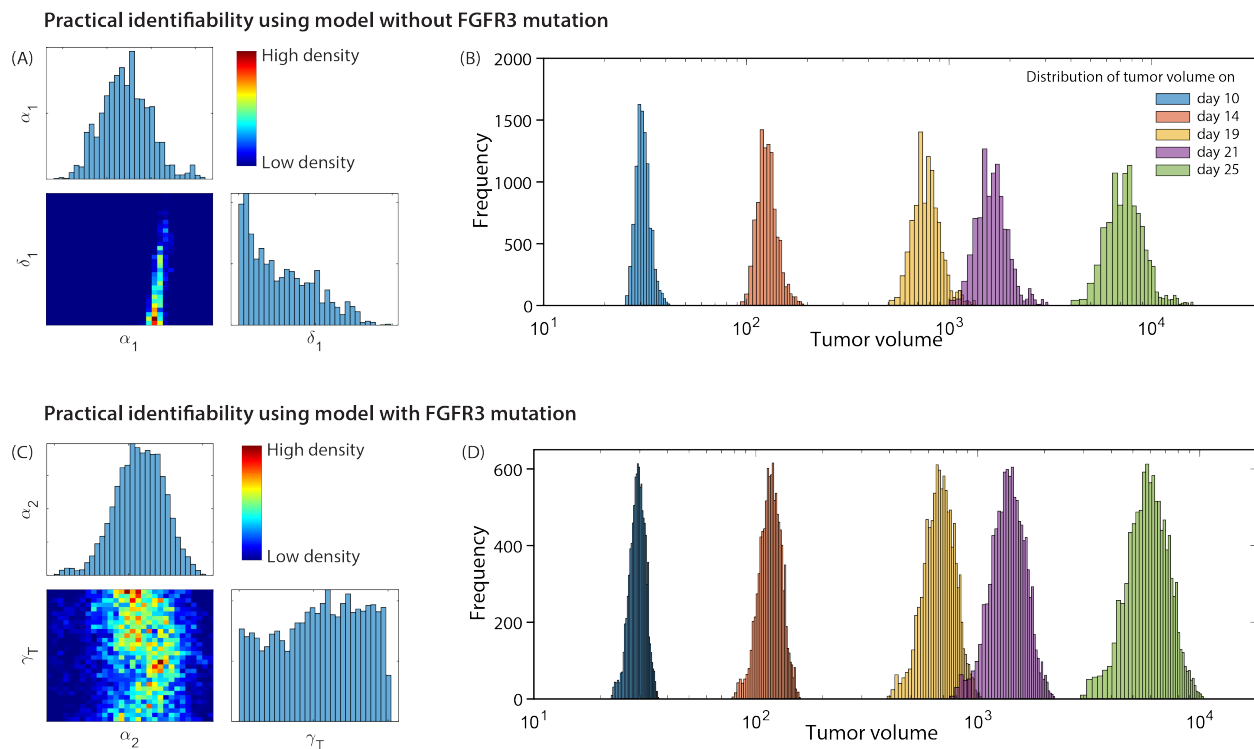


FIGURE 5. (A) Matrix of two-dimensional heat maps with one-dimensional histograms on the diagonal showing the parameter distributions of  $\alpha_1$  and  $\delta_1$  using experimental data of tumor volume without FGFR3 mutation. (B) The distributions of tumor volume for the MCMC chain, for five time points using experimental data of tumor volume without FGFR3 mutation. (C) Matrix of two-dimensional heat maps with one-dimensional histograms on the diagonal showing the parameter distributions of  $\alpha_2$  and  $\gamma_T$  using experimental data of tumor volume with FGFR3 mutation (D) The distributions of tumor volume for the MCMC chain, for five time points using experimental data of tumor volume with FGFR3 mutation.

### 229 3.3 Pretreatment Experimental Studies

230 For mouse experiments, 6-8 week old female C57BL/6 mice were obtained from Jackson laboratory.  
 231 Mice were housed in a specific pathogen-free animal facility at the University of Chicago. The MB49  
 232 cell line is a carcinogen-induced urothelial carcinoma cell line derived from a male C57BL/6 mouse,  
 233 which was generously provided by Timothy L. Ratliff, Purdue University. The MB49-FGFR3G370C  
 234 cell line was generated by retroviral transduction using the pMXs-IRES-GFP vector and sorted  
 235 4 times for GFP expression. For tumor growth experiments, mice were injected subcutaneously with  
 236  $1 \times 10^6$  MB49-FGFR3G370C tumor cells or GFP vector control MB49 tumor cells. Tumor volume  
 237 was measured two times per week until endpoint. All experimental animal procedures were approved

238 by the University of Chicago Animal Care and Use Committee (IACUC).

### 239 **3.4 Pretreatment Parameter Estimation**

240 Having determined the identifiability properties of the most significant parameters both structurally  
241 and practically, we turn to estimating these parameters from experimental data. Specifically, we fit  
242 the mathematical model to two growth curves of MB49 bladder cancer cell lines, with and without  
243 mutant FGFR3 as described above. We use experimental data of tumor volume vs time (5 time  
244 points) for 5 mice without mutant FGFR3 to estimate the FGFR3-independent tumor growth rate  
245 ( $\alpha_1$ ). We use the MATLAB `lsqcurvefit` function with `ode15s` solver, and an initial condition, given  
246 by  $T(0) = 10^6$  cells and  $Y(0) = 3.2 \times 10^5$  cells [11], to carry out the data-fitting process. By  
247 calibrating Equations (3) and (4) with  $\alpha_2 = \gamma_T = 0$  with the experimental data (Figure 6A - green  
248 curve), we obtained the best fit value for  $\alpha_1 = 0.337 \text{ d}^{-1}$ , which corresponds to a bladder tumor  
249 doubling time of 2.1 days in mice. The box-plot of the residual vector shown in Figure 6B indicates  
250 that the model can accurately predict temporal changes tumor volume in mice without the FGFR3  
251 mutation.

252 With FGFR3-independent parameters estimated, we next calibrate the model with FGFR3  
253 mutation (Equations (1), (3), and (4)). Specifically, we use experimental data of tumor volume  
254 vs. time when the FGFR3 mutation is present in mice (Figure 6A - red curve) to estimate two  
255 parameters associated with ligand-independent activation of FGFR3 (i.e., the FGFR3-mediated  
256 tumor proliferation rate ( $\alpha_2 = 0.00774 \text{ d}^{-1}$ ) and the FGFR3-mediated survival sensitivity parameter  
257 ( $\gamma_T = 0.3018$ ). As before, we generated box-plots of residuals (Figure 6C), indicating that the model  
258 can accurately predict tumor volume when the FGFR3 mutation is active. It is important to note  
259 that growth of the experimental tumor cell line is not dependent on the FGFR3 activating mutation,  
260 which was exogenously introduced. Thus, we do not expect the FGFR3 activating mutation to have  
261 a significant impact on tumor growth as observed in both the data and model simulation.

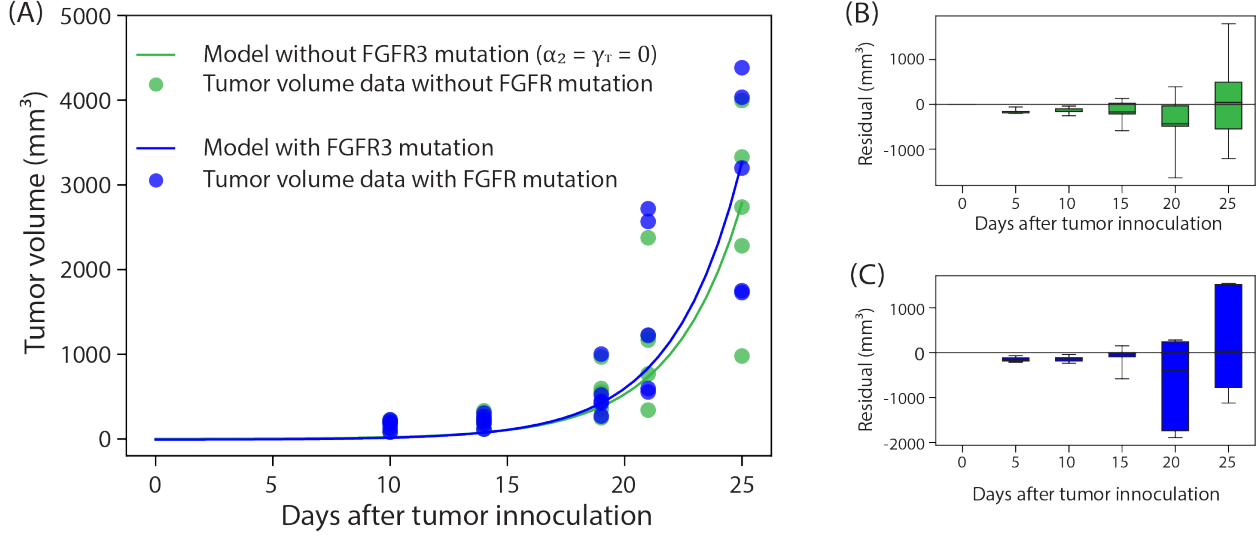


FIGURE 6. (A) Green curve: Calibration of models (3) and (4) with  $\alpha_2 = \gamma_T = 0$  to the experimental data of tumor without FGFR3 mutation in mice ( $n = 5$ ) to estimate the FGFR3-independent growth rate ( $\alpha_1 = 0.337 \text{ d}^{-1}$ ). Blue curve: Calibration of models (1), (3), and (4) to the growth curve of tumor with FGFR3 mutation in mice ( $n = 5$ ) to estimate FGFR3-dependent parameters ( $\alpha_2 = 0.00774 \text{ d}^{-1}$  and  $\gamma_T = 0.3018$ ). (B, C) Residual plots showing that the models predict tumor volume without FGFR3 mutation and with FGFR3 mutation, respectively.

### 262 3.5 Relative Impact of FGFR3-dependent Pathways on Tumor Growth

263 With all parameters associated with tumor growth now estimated, an important question arises  
 264 about which FGFR3-mediated effect, increased proliferation or increased survival, results in a  
 265 greater measurable increase in tumor volume. We addressed this by estimating, from simulations,  
 266 the difference between the tumor volume on day 25 when the FGFR3 survival benefit is switched  
 267 off (i.e.  $\alpha_2 \in [0.001, 0.03]$  and  $\gamma_T = 0$ ) and when the FGFR3 proliferative benefit is turned off (i.e.  
 268  $\alpha_2 = 0$  and  $\gamma_T \in [0.1, 0.5]$ ). In this way, we compare their relative contributions to tumor growth  
 269 and in Figure 7 we see that parameter space is divided in two by which mechanism leads to more  
 270 tumor growth. It is interesting to note that the region in parameter space that corresponds to the  
 271 proliferation effect resulting in larger tumors is much more expansive. This region also contains the  
 272 point corresponding to our estimated parameters as shown by the red dot in Figure 7, though the  
 273 difference in the effect on tumor volume there is slight.

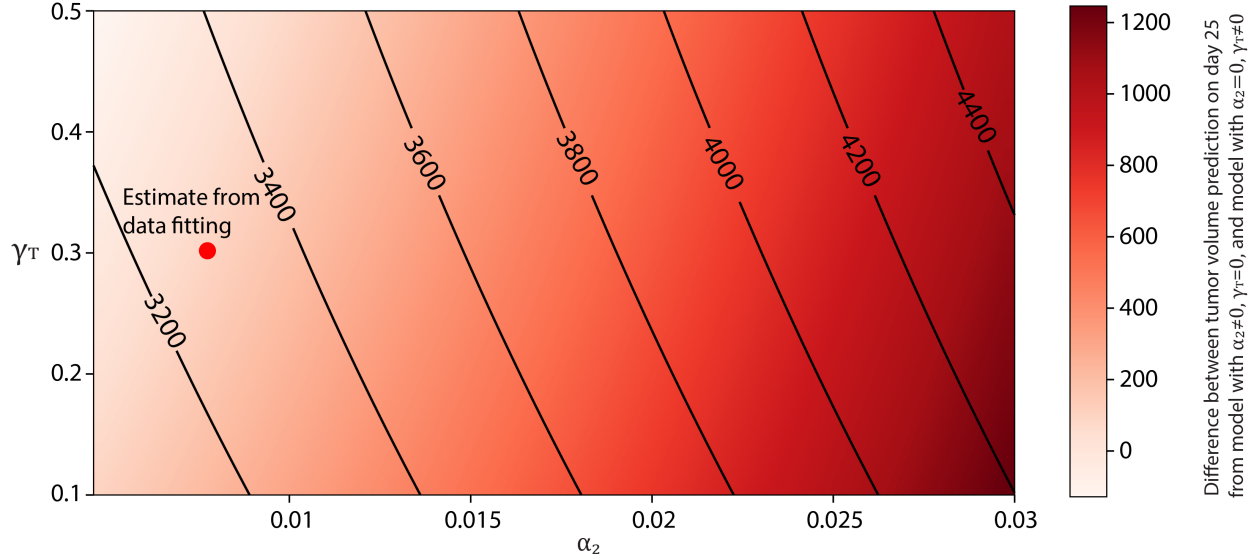


FIGURE 7. Heatmap showing the difference between tumor volume in mice on day 25 predicted from model with  $\alpha_2 \in [0.001, 0.03]$  and  $\gamma_T = 0$  and volume in mice on day 25 predicted from model with  $\alpha_2 = 0$  and  $\gamma_T \in [0.1, 0.5]$ . The red dot represents the difference between the model with  $\alpha_2 = 0.00774 \text{ d}^{-1}$ ,  $\gamma_T = 0$  and the model with  $\alpha_2 = 0 \text{ d}^{-1}$ ,  $\gamma_T = 0.3018$ , indicating that FGFR3 mutation have an almost equal effect on both tumor proliferation and survival in the experimental design. The contour plot shows the prediction of tumor volume on day 25 at the different pairs of  $\alpha_2$  and  $\gamma_T$  in the ranges  $[0.001, 0.03]$  and  $[0.1, 0.5]$ , respectively.

## 274 4 Treatment Results

275 We next turn to the question of understanding the effects of therapy on the tumor reduction.  
 276 Specifically, in this section we simulate the model with immune checkpoint and FGFR3 targeted  
 277 therapy alone and in combination. The dosing schedule for the therapies are presented in Figure 8  
 278 – anti-FGFR3 therapy is administered every day starting from day 7 through day 25 except on days  
 279 12, 13, 19, and 20 (these days are regarded as off-days) and anti-PD-L1 antibody is administered  
 280 every 3 days starting on day 7 (except on the off-days).

	1	2	3	4	5	6	7	8	9	10	11	12	13	14	15	16	17	18	19	20	21	22	23	24	25
Anti-FGFR3							█	█	█	█	█			█	█	█	█	█			█	█	█	█	█
Anti-PDL1							█			█				█			█				█				█

FIGURE 8. Dosing schedule of anti-FGFR3 and anti-PD-L1 monotherapies.

281 **4.1 Treatment with anti-PD-L1 Antibody Alone**

282 In order to study the effect of monotherapy with an anti-PD-L1 immunotherapeutic agent, we cali-  
 283 brated Equations (1), (3), and (9)) with the experimental data for tumor cells without the FGFR3  
 284 mutation in mice (Figure 9A). In the experiments that generated this data, doses of 100  $\mu\text{g}$  anti-  
 285 PD-L1 therapeutic agent with a half-life of 48 hours was administered to mice via intraperitoneal  
 286 injection using the baseline schedule in Figure 8. We used this data to estimate the drug disso-  
 287 ciation constant ( $K_D$ ) and the depletion rate of anti-PD-L1 antibodies through binding to PD-L1  
 288 ( $\mu_{LA}$ ). These results are shown in Fig 9A. With the model now calibrated to data where the FGFR3  
 289 mutation is absent, we turn to validating the model with data where the FGFR3 mutation is active.  
 290 Specifically, to accomplish this validation step, we directly compared (i.e., no additional parameter  
 291 fitting) the model simulations with the experimental data of anti-PD-L1 therapy against FGFR3-  
 292 mutant tumor cells (Figure 9B). The result shows an excellent correlation between the model and  
 293 the data without the need for parameter tuning.

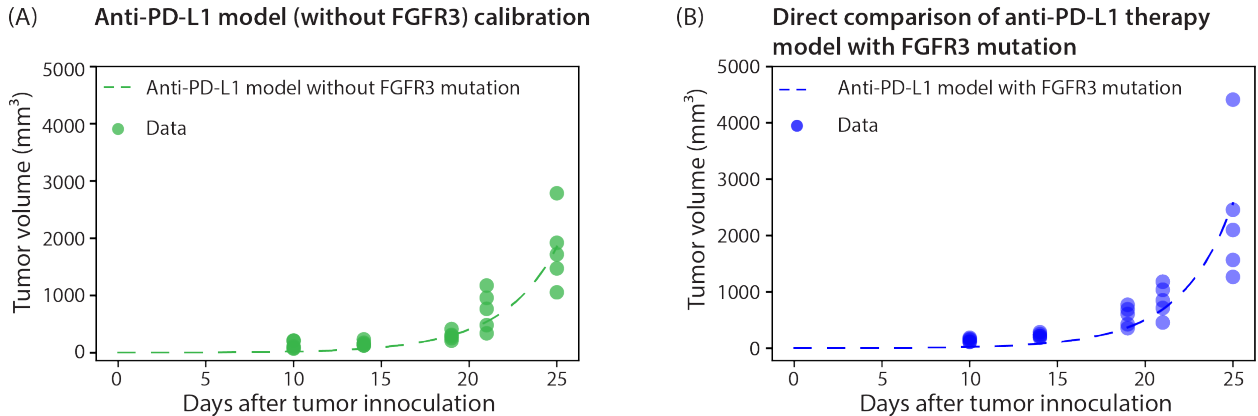


FIGURE 9. (A) Anti-PD-L1 therapy model calibration to experimental data of anti-PD-L1 therapy on tumor cells without FGFR3 mutation in mice to estimate  $K_D = 0.1005 \text{ nM}$ ,  $\mu_{LA} = 2.6611 \times 10^{-5} \text{ d}^{-1}$ . (B) The estimated parameters are used to simulate the anti-PD-L1 therapy model with FGFR3 mutation, and directly compared with the corresponding data in mice. Parameter values used are given in Tables 2 and 4.

294 In Figure 10, the model output from Figures 9A and B is compared to the corresponding models  
 295 without anti-PD-L1 therapy. The larger gap in 10A compared to 10B shows that mice without  
 296 FGFR3 mutation receive more benefit from anti-PD-L1 therapy compared to mice with FGFR3

mutation.

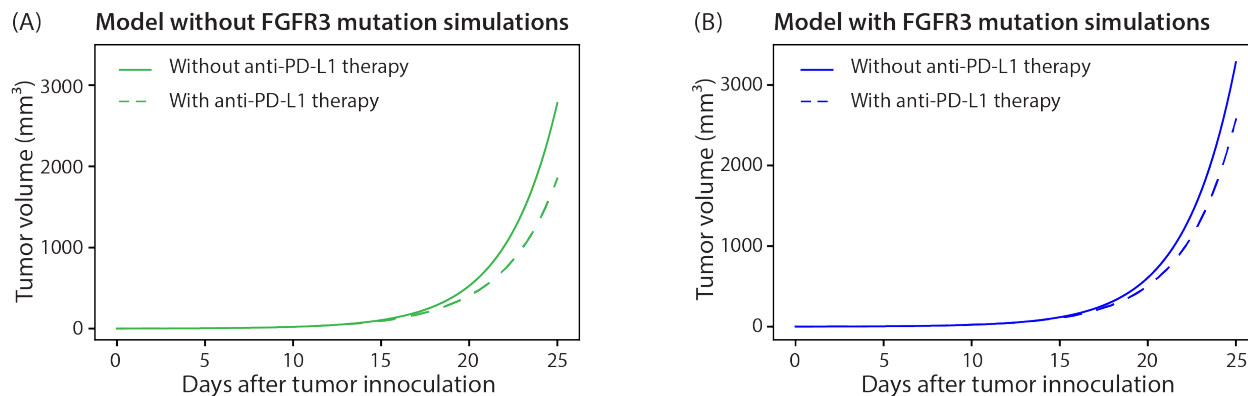


FIGURE 10. Comparison of models with anti-PD-L1 therapy. Results in (A) and (B) show that mice without FGFR3 mutation receive more benefit from anti-PD-L1 therapy compared to mice with FGFR3 mutation. Parameter values used are given in Tables 2 and 4.

297

## 298 4.2 Treatment with anti-FGFR3 Inhibitor Alone

299 Next we investigate targeted therapy against the FGFR3 receptor using the dosing schedule in Figure  
300 8. To estimate rogaratinib pharmacokinetic parameters, we fit a three-compartment model for  
301 rogaratinib bio-distribution (described in Appendix B) to experimental data of rogaratinib plasma  
302 concentration in mice [17]. Using these parameter values, we simulated (see Figure 11) FGFR3  
303 mutant tumor response to the following doses of rogaratinib: 25 mg/kg QD (once a day), 25 mg/kg  
304 BID (twice a day), 50 mg/kg QD, and 75 mg/kg QD using the dosing schedule in Figure 8. It is  
305 clear from Figure 11 that the various doses of anti-FGFR3 drugs do not have substantial impacts on  
306 the tumor volume. Also, the effect sizes of the doses are approximately equal. These results are not  
307 surprising since this tumor cell line is not dependent on the FGFR3 activating mutation—which was  
308 exogenously introduced to study its impact on anti-PD-L1 therapy as shown in Fig 10—for enhanced  
309 tumor growth.

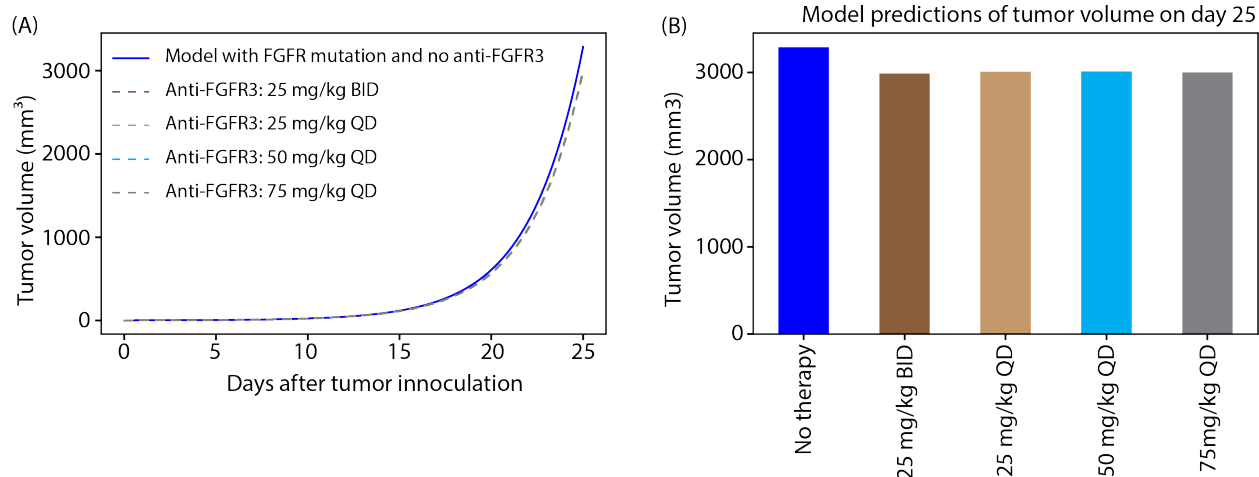


FIGURE 11. Simulation of anti-FGFR3 therapy model with FGFR3 mutation with no treatment, 25 mg/kg QD (once a day), 25 mg/kg BID (twice a day), 50 mg/kg QD, and 75 mg/kg QD of rogaratinib using the dosing schedule in Figure 8. (B) Model prediction of tumor volume on day 25 in mice. Parameter values used are given in Tables 2-4.

### 310 4.3 Treatment with Combination Therapy

311 We simulated the model to predict the effect of combining anti-FGFR3 and anti-PD-L1 therapies on  
 312 tumor cells with FGFR3 mutation in mice (using the dosing schedule in Figure 8 with co-treatment  
 313 on days 7, 10, 14, 17, 21 and 24). The result is shown in Figure 12, along with the impact of  
 314 anti-FGFR3 therapy only and anti-PD-L1 therapy only. Our model predictions show that the effect  
 315 of each therapy is approximately additive when combined, and combination therapy reduces the  
 316 tumor volume on day 25 by 33.3% compared to 21.9% in the case of anti-PD-L1 therapy only.  
 317 Similar results were obtained when the anti-PD-L1 therapy is combined with either 25 mg/kg QD,  
 318 25 mg/kg BID or 50 mg/kg QD dose of rogaratinib (results not shown).

319 We further simulated the model with a wider range of the parameters that govern FGFR3 impact  
 320 on proliferation ( $\alpha_2 \in [0.001, 0.03]$ ) and survival ( $\delta_1 \in [0.1, 0.5]$ ) to compare the effectiveness of anti-  
 321 PD-L1 and anti-FGFR3 monotherapies when the influence of the FGFR3 mutation on tumor growth  
 322 varies. The results depicted in Figure 13 show that for some combinations of  $\alpha_2$  and  $\gamma_T$ , especially in  
 323 the region where the FGFR3 pathway has significant impact on tumor growth, the targeted therapy  
 324 outperforms the immune checkpoint monotherapy (this result also shows the possible significant  
 325 impact of anti-FGFR3 monotherapy on FGFR3 overexpressing cancers). It is also important to

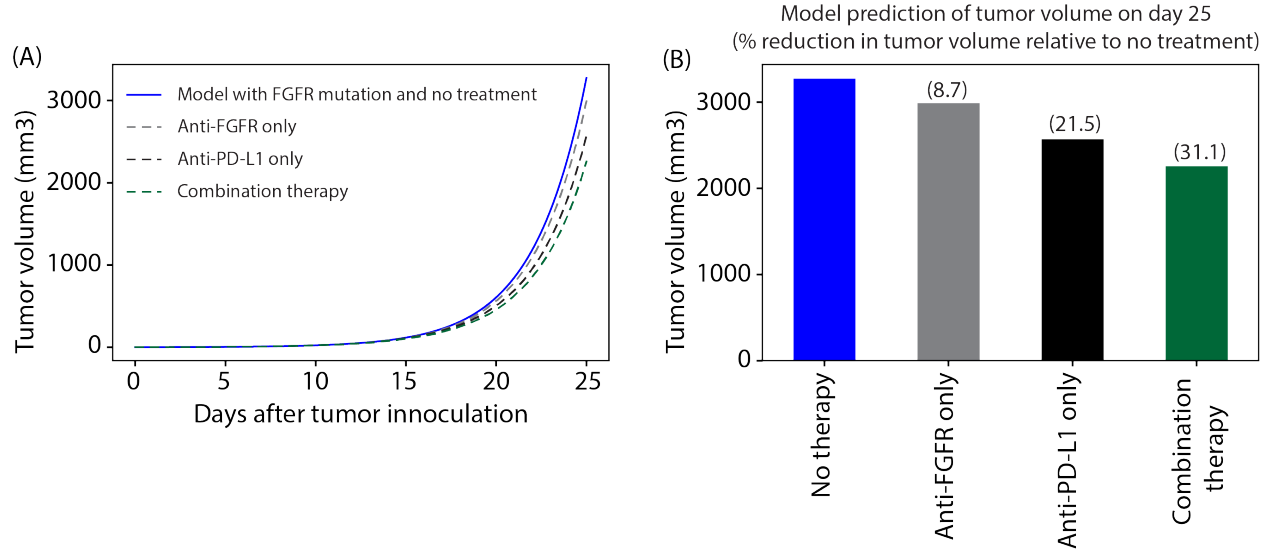


FIGURE 12. (A) Simulation of model with FGFR3 mutation with no therapy (blue), anti-FGFR3 therapy only (gray), anti-PD-L1 therapy only (black) and combination therapy (green). (B) Model prediction of tumor volume on day 25 in mice. Parameter values used are given in Tables 2-4.

326 note, by comparing Figure 12B to Figure 13BII, that the efficacy of combination therapy can be  
 327 significantly increased in parameter ranges where there is a substantial increase in the effectiveness  
 328 of rogaratinib while anti-PD-L1 therapy retains its efficacy.

#### 329 4.4 Kaplan-Meier Survival Analysis

330 Kaplan-Meier survival analysis is used to measure the fraction of subjects living for a certain amount  
 331 of time after treatment in an experiment or clinical trial [29]. To further estimate the effects of anti-  
 332 FGFR3 monotherapy, anti-PD-L1 monotherapy, and combination therapies on tumor with FGFR3  
 333 mutation using the baseline dosing schedule in Figure 8, we carried out a Kaplan-Meier analysis by  
 334 measuring the fraction of mice,  $S_t$ , surviving at time  $t$  using the formula below:

$$S_t = \frac{N - N_{TV \geq 2000 \text{mm}^3, t}}{N}, \quad (12)$$

335 where  $N$  is the total number of mice and  $N_{TV \geq 2000 \text{mm}^3, t}$  is the number of mice that did not survive  
 336 (i.e., mice with tumor volume ( $TV$ ) above or equal to the survival threshold ( $2000 \text{mm}^3$ )) at time  $t$ .  
 337 We generated 50 mice by randomly sampling the sensitive parameters ( $\alpha_1, \delta_T, \alpha_2$ , and  $\gamma_T$ ) within

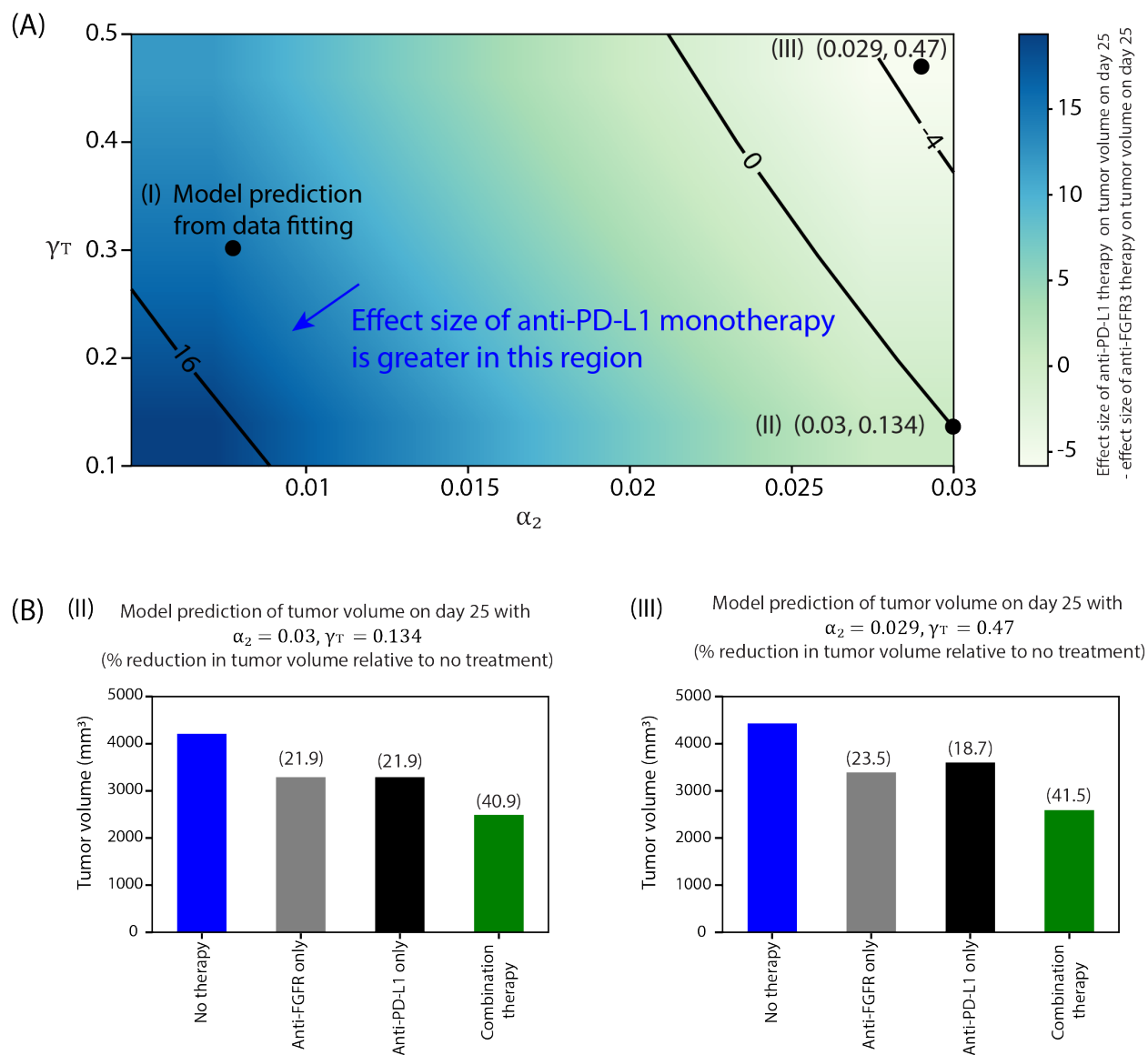
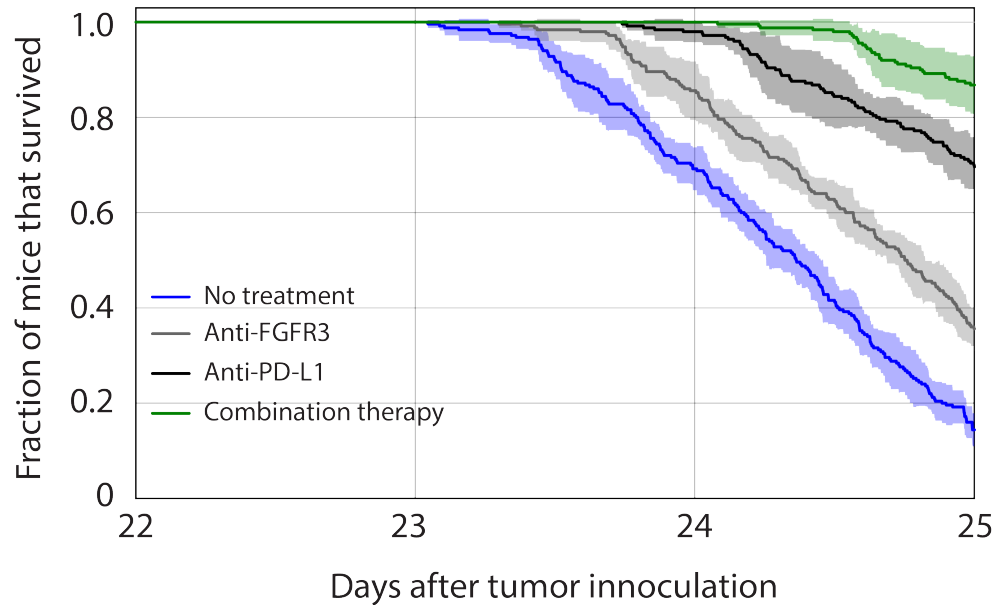


FIGURE 13. (A) A heatmap showing the difference in effect size of anti-PD-L1 and anti-FGFR3 therapies on day 25 on tumor with FGFR3 mutation. The black dot (i) indicate an example where anti-PD-L1 therapy has larger effect size than anti-FGFR3 therapy (the values for the effect sizes are shown in Figure 12B) (B) Prediction of tumor volume and effect size of anti-PD-L1 monotherapy, anti-FGFR3 monotherapy, and combination therapy using (ii)  $\alpha_2 = 0.03 \text{ d}^{-1}$  and  $\gamma_T = 0.134$  where the effect size of anti-PD-L1 and anti-FGFR3 are approximately equal; and (iii)  $\alpha_2 = 0.029 \text{ d}^{-1}$  and  $\gamma_T = 0.47$  where anti-PD-L1 therapy has lesser effect size than anti-FGFR3 therapy. The arrow indicates the direction of increasing relative strength of anti-PD-L1 monotherapy.

338 their ranges of values given in Table 2. In particular, we generated normal sampling distributions for  
 339 practically identifiable parameters ( $\alpha_1$  and  $\alpha_2$ ) using their respective mean and standard deviation

340 and uniform sampling distributions for practically non-identifiable parameters ( $\delta_1$  and  $\gamma_T$ ). The  
 341 simulation was repeated for five stochastic realizations. The result depicted in Figure 14 shows that  
 342 78 – 96% of the mice treated with combination therapy survived on day 25 compared to mice treated  
 343 with anti-PD-L1 monotherapy (62 – 76%), anti-FGFR3 monotherapy (28 – 42%) or untreated mice  
 344 (10 – 20%). Since the values for the FGFR3-dependent parameters are within the region where anti-  
 345 PD-L1 monotherapy has more effect size than anti-FGFR3 monotherapy (Figure 13A), we expect  
 that more mice would survive when treated with anti-PD-L1 therapy.



Mean number of mice at risk

No treatment	50	34	7
Anti-FGFR3	50	42	18
Anti-PD-L1	50	49	34
Combination therapy	50	50	43

FIGURE 14. Kaplan-Meier survival analysis showing the fraction (mean  $\pm$  SD) of mice that survived with no treatment (blue), anti-FGFR3 monotherapy (gray), antiPD-L1 monotherapy (black) and combination therapy (green). Parameter values used are in Tables 2-4 with normal distribution of  $\alpha_1$  (with mean =  $0.337 \text{ d}^{-1}$  and standard deviation =  $0.0034 \text{ d}^{-1}$ ), normal distribution of  $\alpha_2$  (with mean =  $0.00774 \text{ d}^{-1}$  and standard deviation =  $0.0016 \text{ d}^{-1}$ ), uniform distributions of  $\delta_1$  and  $\gamma_T$  within their range of values in Table 2

346

347 Figure 15 shows the distribution of parameters associated with the mice that survived until day

348 25 in the Kaplan-Meier survival analysis. These results show that the surviving mice are character-  
 349 ized by high CTL-induced death rate ( $\delta_1$ ) (i.e., slow-growing tumor cells). In particular, the only  
 350 untreated mice that survived until day 25 had a CTL-induced death rate above  $1.9 \times 10^{-7} \text{cell}^{-1} \text{d}^{-1}$ ;  
 351 those treated with anti-FGFR3 monotherapy needed at least a value of  $1.6 \times 10^{-7} \text{cell}^{-1} \text{d}^{-1}$  (with  
 352 one exception). Even anti-PD-L1 monotherapy and combination therapy needed  $\delta_1$  to exceed  
 353  $1.3 \times 10^{-7} \text{cell}^{-1} \text{d}^{-1}$  to give at least even odds for the mice to survive until day 25.

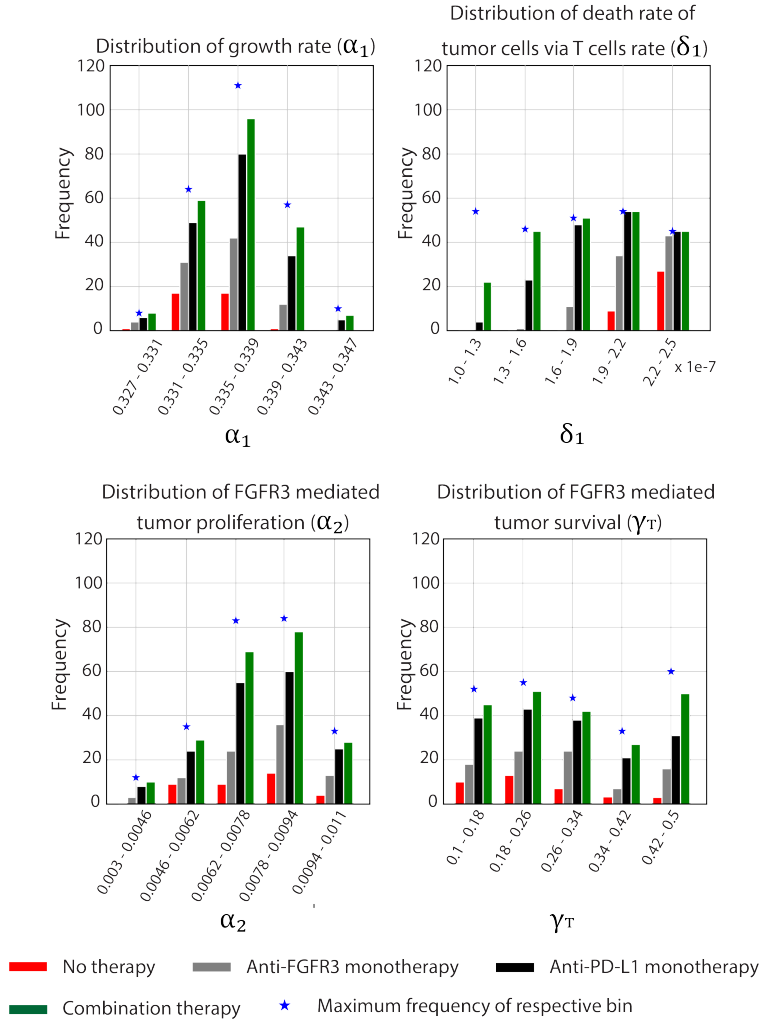


FIGURE 15. Distribution of sensitive parameters related to mice that survived on day 25 of survival analysis with different therapeutic conditions. The distances between each bar and the maximum frequency represent the distribution of mice that did not survive in the Kaplan-Meier analysis.

354 **4.5 Dosing Schedules**

355 Next, we use the model to determine how best to administer anti-PD-L1 and anti-FGFR3 targeted  
 356 therapies. To determine the most favorable combinations and to investigate the potential synergy  
 357 between anti-PD-L1 and anti-FGFR3 therapies in mice with FGFR3 mutation, we simulate different  
 358 dose-scheduling for anti-FGFR3 and anti-PD-L1 therapies (Figure 16).

**Schedule 2: Pretreatment with RTK Targeted Therapy**

	1	2	3	4	5	6	7	8	9	10	11	12	13	14	15	16	17	18	19	20	21	22	23	24	25
Anti-FGFR3							█	█	█	█	█			█	█	█	█	█							
Anti-PDL1														█			█				█			█	

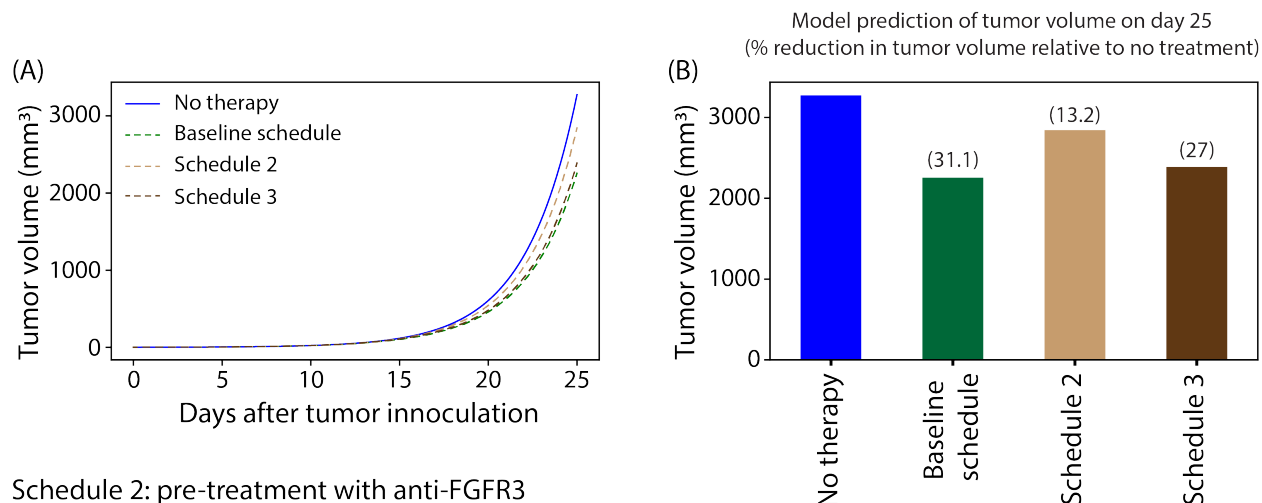
**Schedule 3: Pretreatment with Immune Checkpoint Therapy**

	1	2	3	4	5	6	7	8	9	10	11	12	13	14	15	16	17	18	19	20	21	22	23	24	25
Anti-FGFR3														█	█	█	█	█			█	█	█	█	█
Anti-PDL1							█			█				█			█								

FIGURE 16. Dosing schedule of pretreatment with anti-FGFR3 therapy and pretreatment with anti-PD-L1 therapy.

359 In these simulations, we considered treatments of tumor cells with FGFR3 mutation with a total  
 360 of 10 doses of 75 mg/kg QD of rogaratinib and 4 doses of 100 μg of anti-PD-L1 antibody using the  
 361 dosing schedules 2 and 3 shown in Figure 16 (compared to 15 doses of anti-FGFR3 and 6 doses of  
 362 anti-PD-L1 in the dosing schedule (baseline schedule) in Figure 8).

363 The ultimate goal is to determine the optimal dosing strategy that minimizes tumor growth  
 364 while also minimizing the amount of drug administered. The tumor is either pretreated with anti-  
 365 FGFR3 therapy or pretreated with anti-PD-L1 therapy as shown in Figure 17. The results depicted  
 366 in Figures 17 show that the pretreatment of tumors with anti-PD-L1 therapy (Schedule 3) is more  
 367 effective than pretreatment of tumors with anti-FGFR3 therapy (Schedule 2). This result persists  
 368 throughout the  $\alpha_2 - \gamma_T$  parameter space, even in regions where anti-FGFR3 monotherapy greatly  
 369 outperforms immune checkpoint monotherapy (result not shown). It is also important to note that  
 370 that the outcomes for Schedule 3 are comparable to those from the baseline schedule of co-treatment,  
 371 which administers five additional doses of therapy.



Schedule 2: pre-treatment with anti-FGFR3

Schedule 3: pre-treatment with anti-PDL1

FIGURE 17. Simulation showing effect size of the different dosing schedules (A) Simulation of model with FGFR3 mutation with no therapy (blue), treatment with baseline combination therapy (green), pretreatment with anti-FGFR3 therapy, and pretreatment with anti-PD-L1 therapy. (B) Model prediction of tumor volume on day 25 in mice. Parameter values used are given in Tables 2-4.

## 5 Discussion

Until recently, systemic chemotherapy was the only recourse for people suffering from bladder cancer, and outcomes remained discouraging as many patients either fail to respond to treatment or suffer recurrent disease within 5 years [30, 31]. After nearly four decades of little progress, immunotherapy with checkpoint inhibitors (PD-L1 and PD-1) has fundamentally shifted the treatment paradigm of bladder cancer [31]. At the same time, advances in the understanding of the molecular biology of bladder cancer has led to the identification of molecular pathways, such as FGFR3 signaling, upon which new therapeutic approaches can be targeted [32]. In this paper, we developed an experimentally-validated mathematical model for the dynamics of bladder cancer growth and response to receptor tyrosine kinase (RTK) targeted therapy alone and in combination with an immune checkpoint inhibitor (ICI). This model is the first of its kind in that it incorporates the molecular details of an FGFR3 mutation that initiates signaling via ligand-independent dimerization to enhance tumor cell proliferation and survival. Our model formulation allows us to track the fraction of active FGFR3 dimers and to use this quantity to augment the rates of tumor cell

386 division and tumor cell death, which is mediated by cytotoxic T cells. A second important feature  
387 of our model is that it explicitly accounts for the formation of PD-1/PD-L1 complexes that inhibit  
388 T cell proliferation and activation.

389 The model is carefully calibrated and validated with experimental measures of tumor volume  
390 with and without the FGFR3 mutation. In an attempt to identify which FGFR3-mediated effect  
391 has more impact on tumor growth, we computed the difference between the tumor volume when  
392 FGFR3 only impacts the tumor cell proliferation rate and the tumor volume when FGFR3 only  
393 impacts tumor cell survival. The results suggest that FGFR3 mutation can lead to increased tumor  
394 volume due primarily to either proliferation or survival effects—depending on the relative strengths  
395 of these signaling pathways, i.e. the parameters. However, the proliferation effect is more influential  
396 across a larger region of parameter space. Interestingly, for our estimated parameter values, the  
397 effects of FGFR3 on proliferation and survival are nearly equal.

398 Based on the mechanisms of action of an immune checkpoint inhibitor targeting PD-L1 and a  
399 tyrosine kinase inhibitor targeting FGFR3 (rogaratinib), we extended our model to evaluate the  
400 impact of these therapies alone and in combination. Simulations of anti-PD-L1 therapy showed  
401 that tumors with FGFR3 mutation are more susceptible to anti-PD-L1 therapy than wild type  
402 FGFR3 tumors. This effect is likely independent of FGFR3 effects on intrinsic tumor growth and  
403 survival, since both cell lines grow essentially at the same rate in the presence or absence of FGFR3  
404 activating mutations. These results are in line with our reported experimental data and suggest  
405 that the FGFR3 mutation can impact the effectiveness of anti-PD-L1 therapy. Furthermore, the  
406 experiments described here use a tumor cell line that is not dependent on the FGFR3 activating  
407 mutation, which was exogenously introduced. Thus, we did not expect the FGFR3 activating  
408 mutation to have a significant impact on tumor growth. Our anti-FGFR3 monotherapy model  
409 simulations clearly show that this is indeed the case for four different doses of rogaratinib. However,  
410 when we simulated a wider range of the parameters that govern FGFR3 impact on proliferation  
411 and survival, we saw that for realistic values of  $\alpha_2$  and  $\gamma_T$ , anti-FGFR3 therapy can not only  
412 have substantial impact on tumor reduction, targeted therapy can actually outperform anti-PD-L1  
413 monotherapy.

414 Despite the slight impact of rogaratinib monotherapy on tumor cells with FGFR3 mutation when  
415 baseline parameters are used, our model simulations show that its combination with anti-PD-L1  
416 therapy increases the effect size of the anti-PD-L1 therapy on tumor cells with the FGFR3 mutation.  
417 That is, while anti-PD-L1 antibody loses efficacy when the FGFR3 mutation is active, anti-PD-L1  
418 antibody impact on tumor reduction is recovered when combined with a drug that targets FGFR3.  
419 In fact, Kaplan-Meier survival analysis showed that when mice with FGFR3 mutant bladder cancer  
420 are treated with combination therapy, they have a much higher probability of surviving to day 25  
421 compared to mice treated with either monotherapy. We also found that there are parameter ranges  
422 for  $\alpha_2$  and  $\gamma_T$  where there is a significant increase in tumor reduction due to rogaratinib and  
423 only a small decrease in tumor reduction due to immune checkpoint therapy, and this leads to a  
424 substantial increase in the efficacy of combination therapy.

425 In an attempt to find the most effective way of delivering combinations of these two therapies , we  
426 simulated two different dose-scheduling regimens for rogaratinib and an immune checkpoint inhibitor  
427 targeting PD-L1. We compared outcomes of these strategies to each other and to our baseline dose  
428 schedule of co-treatment, which administers five additional doses of rogaratinib. Our results show  
429 that pretreatment with anti-PD-L1 therapy leads to greater tumor reduction than pretreatment  
430 with anti-FGFR3 therapy. Interestingly, even in parameter regimes where anti-FGFR3 monotherapy  
431 greatly outperforms immune checkpoint monotherapy, the model predicts that it is still better to  
432 pretreat with the anti-PD-L1 drug. Furthermore, our baseline schedule of co-treatment performs  
433 only slightly better, with five additional doses of anti-PD-L1 therapy, than pretreatment with anti-  
434 PD-L1 therapy. This result suggests that some patients may benefit more from pretreatment with  
435 anti-PD-L1 because fewer drug doses can be used to achieve similar outcomes. These findings have  
436 direct clinical relevance given that anti-FGFR3 therapy is currently FDA approved, but it remains  
437 unknown whether it is best employed prior to or after anti-PD-L1 immunotherapy.

438 This modeling study not only quantifies the influence of the FGFR3 mutation on bladder cancer  
439 growth; it also predicts various outcomes for RTK and ICI mono- and combination therapy. In the  
440 current model formulation, we are considering the total amount of FGFR3 monomers in the system  
441 and allowing all monomers to interact with each other. The resulting dimerization of monomers

442 allows us to quantify the temporal changes in fractional occupancy of active FGFR3 dimers in the  
443 system and their impact on tumor growth dynamics. In future iterations of the model, we could  
444 relax these assumptions and reformulate the model so that FGFR3 monomers only interact with  
445 other monomers on the same cell. We are currently modifying this model to describe different  
446 mechanisms of immune cell kill. We will also extend the model to include the impact of spatial  
447 dynamics by translating this system of ordinary differential into an agent-based modeling framework.  
448 Continued computational modeling of bladder cancer therapy can potentially lead to patient specific  
449 optimization of combination of anti-FGFR3 with anti-PD-L1 treatments.

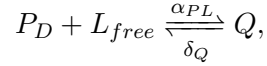
450 **Appendix**

451 **A. Formulation for PD-1/PD-L1 Complexes,  $Q$**

Following [12], the molar concentration of PD-L1 ( $L$ ) within the tumor microenvironment consists of the amount of free PD-L1 and the amount of PD-L1 bound to the drug,

$$L = L_{free} + L_{bound},$$

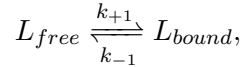
with  $L = \rho_L(Y + \epsilon T)$ . We consider the following reaction:



452 Following [10, 12, 13, 16], we assume that the association and dissociation of  $Q$  are fast, so  
 453 applying a quasi-steady state argument, we can approximate  $Q$  using the equation:

$$Q = \frac{\alpha_{PL}}{\delta_Q} P_D L_{free} = \frac{\alpha_{PL}}{\delta_Q} P_D (L - L_{bound}). \quad (\text{A-1})$$

We also considered the following reaction:



454 where  $k_{+1}$  and  $k_{-1}$  are the association and dissociation rates of  $L_{bound}$ . By the law of mass action  
 455 and assuming the process is at equilibrium [12],

$$\begin{aligned} \frac{dL_{bound}}{dt} &= k_{+1} L_{free} A - k_{-1} L_{bound} = 0 \\ L_{bound} &= \frac{k_{+1}}{k_{-1}} L_{free} A = \frac{k_{+1}}{k_{-1}} (L - L_{bound}) A \\ L_{bound} &= \frac{A}{A + K_D} L \end{aligned} \quad (\text{A-2})$$

where  $K_D = \frac{k_{-1}}{k_{+1}}$  (i.e., the dissociation constant of the PD-L1/anti-PD-L1 complex). Thus, by substituting Equation (A-2) into Equation (A-1), we derived the following expression for  $Q$ , given

by:

$$Q = \frac{\alpha_{PL}}{\delta_Q} P_{DL} \left( 1 - \frac{A}{A + K_D} \right)$$

456 Finally, we choose the following functional form for  $F(Q)$  defined by

$$F(Q) = \frac{1}{1 + \frac{Q}{K_{TQ}}} \quad \equiv \quad F(P, L, A) = \frac{1}{1 + \frac{P_{DL}}{K_{YQ}} \left( 1 - \frac{A}{A + K_D} \right)} \quad (\text{A-3})$$

where  $K_{YQ} = \frac{\delta_Q}{\alpha_{PL}} K_{TQ}$  (described in Table 2) [10, 12, 13, 16]. In order to achieve agreement between the units for  $A$  and  $K_D$  in Equation A-3, we converted the dosage of anti-PD-L1 in the experiment from  $\mu\text{g}$  to  $\text{nmol/L}$  using the following formula:

$$c(\text{nmol/L}) = \frac{m(\mu\text{g})}{V(\text{L}) \times \text{molar mass}(\mu\text{g/nmol})},$$

457 where  $V$  is the carrying capacity of tumor volume without FGFR3 mutation ( $4000 \text{ mm}^3 = 0.004 \text{ L}$ ),  
 458 molar mass =  $1.5 \times 10^5 \text{ g/mol} = 1.5 \times 10^2 \mu\text{g/nmol}$ , so that  $100 \mu\text{g}$  of anti-PD-L1 is equivalent to  
 459  $166.67 \text{ nmol/L}$  of anti-PD-L1.

## 460 B. Pharmacokinetics of anti-FGFR3 (rogaratinib)

461 We developed a compartmental model to describe the pharmacokinetic profile of rogaratinib in the  
 462 plasma. The pharmacokinetic model is given as follows, where  $G(t)$ ,  $C_S(t)$ , and  $C_P(t)$  represents  
 463 the concentration of the drug in the gut, central, and peripheral compartments, respectively:

$$\begin{aligned} \frac{dG}{dt} &= k_a G \\ \frac{dC_S}{dt} &= F k_a G - k_{12} C_S + k_{21} C_P - k C_S \\ \frac{dC_P}{dt} &= k_{12} C_S - k_{21} C_P \end{aligned} \quad (\text{B-1})$$

464 where  $k_a$  is the first-order absorption rate constant,  $k$  is the elimination rate constant,  $F$  is the  
 465 bioavailability of the drug that accounts for the fraction of dose that reaches the central compart-  
 466 ment, and  $k_{12}$  and  $k_{21}$  are distribution rate constants from the central compartment to the peripheral

467 compartment and vice versa, respectively. The pharmacokinetic parameters are estimated by fit-  
 468 ting the analytical solution of the central compartment,  $(C_S(t))$  to the experimental data of the oral  
 469 administration of rogaratinib described in [17]. The best fit values and fitting are given in Table  
 470 Table 3 and Figure 18, respectively.

TABLE 3. Best fit pharmacokinetic parameter of rogaratinib for PK model (B-1)

Parameter	Description	Best fit values			Reference
		75 mg/kg	50 mg/kg	25 mg/kg	
$k_a$	Absorption rate	$0.4815 \text{ h}^{-1}$	$0.3597 \text{ h}^{-1}$	$0.4942 \text{ h}^{-1}$	Estimated
$F$	Bioavailabilty	$0.42 \text{ h}^{-1}$	$0.42 \text{ h}^{-1}$	$0.42 \text{ h}^{-1}$	[19]
$k_{12}$	Plasma-Tissue transfer rate	$577.44 \text{ h}^{-1}$	$423.11 \text{ h}^{-1}$	$47.915 \text{ h}^{-1}$	Estimated
$k_{21}$	Tissue-Plasma transfer rate	$1.2478 \text{ h}^{-1}$	$2.6785 \text{ h}^{-1}$	$0.2864 \text{ h}^{-1}$	Estimated
$k$	Elimination rate	$193.53 \text{ h}^{-1}$	$202.95 \text{ h}^{-1}$	$309.15 \text{ h}^{-1}$	Estimated

471

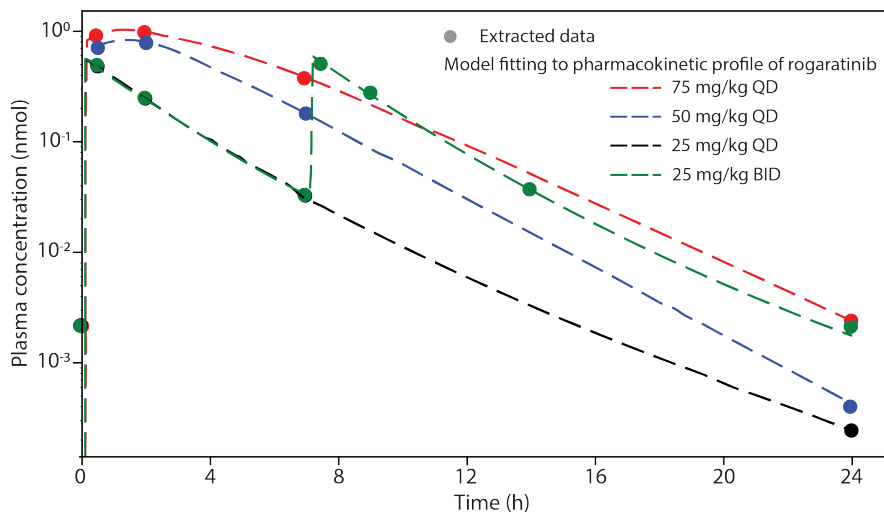


FIGURE 18. Time profiles of single-dose of 75 mg/kg QD (red dashed line), 50 mg/kg QD (blue dashed line), 25 mg/kg QD (black dashed line) and 25 mg/kg BID (green dashed line) of rogaratinib in plasma. The best fit of model is plotted together with experimental data of rogaratinib in mice described in [17]. Parameter values used are given in Tables 2-4.

472 **C. Model equations related to treatment with anti-FGFR3 (rogaratinib)**

473 The system of equations governing the dynamics of the FGFR3 monomers and dimers (see Figure  
474 19) in the tumor cell in the presence of rogaratinib is given by,

$$\begin{aligned}
\frac{dR_F}{dt} &= -2k_f R_F^2 + 2k_r D_A + 2k_p (D_A + D_C^C + D_A^C) + R_T P(T, \phi_D) - k_{c,on}^R C R_F + k_{c,off}^R R_F^C \\
&\quad - \frac{R_F}{\Sigma} R_T D(T, Y, \phi_D^C), \\
\frac{dD_A}{dt} &= k_f R_F^2 - k_r D_A - k_p D_A - k_{c,on}^D C D_A + k_{c,off}^D D_A^C - \frac{D_A}{\Sigma} R_T D(T, Y, \phi_D^C), \\
\frac{dC}{dt} &= k_{12} C_1 - k_{21} C - k_{c,on}^R C R_F + k_{c,off}^R R_F^C - k_{c,on}^D C D_A + k_{c,off}^D D_A^C, \\
\frac{dR_F^C}{dt} &= k_{c,on}^R C R_F - k_{c,off}^R R_F^C - 2k_f (R_F^C)^2 + 2k_r D_C^C - \frac{R_F^C}{\Sigma} R_T D(T, Y, \phi_D^C), \\
\frac{dD_C^C}{dt} &= k_f (R_F^C)^2 - k_r D_C^C - k_p D_C^C - \frac{D_C^C}{\Sigma} R_T D(T, Y, \phi_D^C), \\
\frac{dD_A^C}{dt} &= k_{c,on}^D C D_A - k_{c,off}^D D_A^C - k_p D_A^C - \frac{D_A^C}{\Sigma} R_T D(T, Y, \phi_D^C),
\end{aligned} \tag{C-1}$$

475 where  $R_F$ ,  $D_A$ ,  $R_F^C$ , and  $D_A^C$  represent the free FGFR3 monomers, active dimers, monomer/rogaratinib  
476 complex, and active dimer/rogaratinib complex respectively (see Figure 2 for the flowchart of the  
477 mechanism of action of rogaratinib). The monomer/rogaratinib complexes dimerize to form  $D_C^C$ ,  
478 and  $C$  represents the concentration of rogaratinib in the tumor microenvironment. As an anti-  
479 FGFR3 drug, we assumed that rogaratinib binds to the kinase region of FGFR3 monomers ( $R_F$ )  
480 and active dimers ( $D_A$ ) on tumor cells at rates  $k_{c,on}^R$  (to form monomer/rogaratinib complex ( $R_F^C$ ))  
481 and  $k_{c,on}^D$  (to form active dimer/rogaratinib complex ( $D_A^C$ )). These complexes dissociate at rates  
482  $k_{c,off}^R$  and  $k_{c,off}^D$ , respectively. Furthermore, we assume that rogaratinib drug does not affect dimer-  
483 ization, dissociation, and internalization, thus, the monomer/rogaratinib complex ( $R_F^C$ ) dimerizes  
484 at a rate  $k_f$  to form  $D_C^C$  which can either dissociate at a rate  $k_r$ , internalized at a rate  $k_p$ . We  
485 assumed that upon internalization, both monomer/rogaratinib and active dimer/rogaratinib com-  
486 plexes are recycled at a rate  $k_p$ , leaving behind the drug, to reproduce FGFR3 monomers ( $R_F$ ).  
487 The term  $\phi_D^C$  is the fractional occupancy of active dimer on a tumor cell with anti-FGFR3 and  
488  $\Sigma = R_F + 2D_A + R_F^C + 2D_C^C + 2D_A^C$ . The flowchart and parameter values for model (C-1) are given  
489 in Table 4 and Figure 19, respectively.

The underlying assumptions for this equation are (i) the tumor resides in a pharmacokinetic compartment of its own; (ii) the binding rates are the same, independent of cell type; (iii) rogaratinib is transferred into the tumor from the systemic circulation at the same rate as the peripheral tissue,  $k_{12}$ ; and (iv) the tumor volume is negligible compared to the volume of a mouse; therefore the amount of the drug leaking into the bloodstream (at the rate  $k_{21}$ ) will not affect the concentration of free rogaratinib in the systemic circulation. Furthermore, the formulation of the model (C-1) assumes that the total number (converted to nmol using molecular weight) of receptors per tumor cell  $R_T$  remains constant. Thus, we can ensure that the model equations do conserve FGFR3 by considering the sum:

$$\frac{dR_F}{dt} + 2\frac{dD_A}{dt} + \frac{dR_F^C}{dt} + 2\frac{dD_C^C}{dt} + 2\frac{dD_A^C}{dt} = \frac{d\Sigma}{dt} = R_T (P(T, \phi_D^C) - D(T, Y, \phi_D^C)) = R_T \frac{dT}{dt}.$$

490 Therefore, upon integration, we have  $\Sigma = R_T \times T$ .

TABLE 4. Parameter Values Related to anti-FGFR3 and anti-PD-L1 Therapy

Parameter	Description	Baseline Value	Units	Reference
Anti-FGFR3 related				
$k_{c,on}^R$	Rogaratnib-FGFR3 monomer association rate	$1.28 \times 10^5$	$\text{nmol}^{-1} \text{d}^{-1}$	[17]
$k_{c,off}^R$	Rogaratnib-FGFR3 monomer dissociation rate	95.04	$\text{d}^{-1}$	[17]
$k_{c,on}^D$	Rogaratnib-FGFR3 dimer association rate	$1.28 \times 10^5$	$\text{nmol}^{-1} \text{d}^{-1}$	[17]
$k_{c,off}^D$	Rogaratnib-FGFR3 dimer dissociation rate	95.04	$\text{d}^{-1}$	[17]
Anti-PD-L1 related				
$\mu_{LA}$	Anti-PD-L1 depletion via binding to PD-L1	$2.66 \times 10^{-5}$	$\text{nM}^{-1} \text{d}^{-1}$	Estimated
$\delta_A$	Anti-PD-L1 natural degradation rate	0.3466	$\text{d}^{-1}$	Estimated
$K_D$	PD-L1-Anti-PD-L1 dissociation rate	0.1005	nM	Estimated

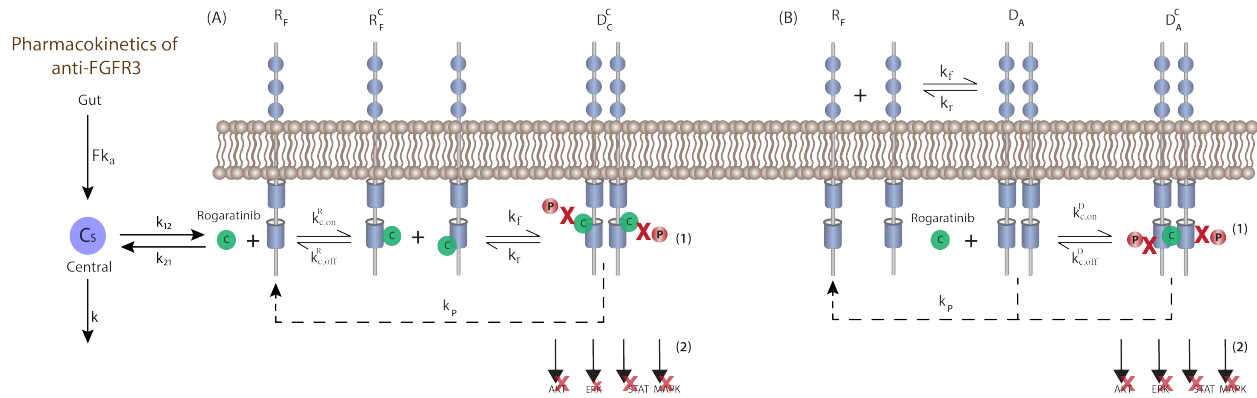


FIGURE 19. Flowchart of rogaratinib as anti-FGFR3 treatment. (A) Rogaratinib drug associate with FGFR3 monomer on tumor cells at a rate  $k_{C,on}^R$  to form  $R_F^C$  and dissociate at a rate  $k_{C,off}^R$ .  $R_F^C$  dimerize at a rate  $k_f^C$  to form  $D_C^C$  which can either dissociate at rate  $k_r$ , or internalize and recycled into FGFR3 monomer at a rate  $k_p$ . (B) Rogaratinib bind with an active dimer  $D_A$  at a rate  $k_{C,on}^D$  to form  $D_A^C$  which dissociate at a rate  $k_{C,off}^D$ . These events lead to (1) inhibition of FGFR3 phosphorylation; and consequently, (2) inhibition of downstream signaling of AKT, MAPK, ERK and STAT.

## References

- [1] Siegel R, Miller K, Jemal A. 2020 Cancer statistics, 2020. CA Cancer J Clin **70**, 1, 7–30.
- [2] Raghavan D. 2015 Chemotherapy for invasive bladder cancer: Five simple rules learned over 30 years. Bladder Cancer **1**, 1, 3–13.
- [3] Chang J, Lara P, Pan CX. 2012 Progress in personalizing chemotherapy for bladder cancer. Adv in Urol **2012**. (doi:10.1155/2012/364919).
- [4] Casadei C, Dizman N, Schepisi G, Cursano M, Basso U, Santini D, Pal S, Giorgi UD. 2019 Targeted therapies for advanced bladder cancer: new strategies with fgfr inhibitors. Ther Adv Med Oncol **11**. (doi:10.1177/1758835919890285).
- [5] Sheepbouwer C, Meyer S, Burggraaf J, Jose J, Molhoff C. 2016 A multimodal imaging approach for longitudinal evaluation of bladder tumor development in an orthotopic murine model. PLoS ONE **11**, 8, e0161284.
- [6] Qin W, Hu L, Zhang X, Jiang S, Lj J, Zhang Z, Wang X. 2019 The diverse function of pd-1/pd-l1 pathway beyond cancer. Front Immunol **10**, 2298. (doi:10.3389/fimmu.2019.02298).

- 506 [7] Hsu F, Su C, Huang K. 2017 A comprehensive review of us fda-approved immune checkpoint  
507 inhibitors in urothelial carcinoma. J Immuno Res **2017**. (doi:https://doi.org/10.1155/2017/  
508 6940546).
- 509 [8] Kacew A, Sweis RF. 2020 Fgfr3 alterations in the era of immunotherapy for urothelial bladder  
510 cancer. Front Immunol **11**, 575258. (doi:doi:10.3389/fimmu.2020.575258).
- 511 [9] Jain HV, Jackson TL. 2018 Mathematical modeling of cellular cross-talk between endothelial  
512 and tumor cells highlights counterintuitive effects of vegf-targeted therapies. Bull Math Biol  
513 **80**, 5, 971–1016. (doi:10.1007/s11538-017-0273-6).
- 514 [10] Storey KM, Lawler SE, Jackson TL. 2020 Modeling oncolytic viral therapy, immune check-  
515 point inhibition, and the complex dynamics of innate and adaptive immunity in glioblastoma  
516 treatment. Front Physiol **11**, 151. (doi:10.3389/fphys.2020.00151).
- 517 [11] Kuznetsov V, Makalkin I, Taylor M, Perelson A. 1994 Nonlinear dynamics of immunogenic  
518 tumors: parameter estimation and global bifurcation analysis. Bull Math Biol **52**, 2, 295–321.
- 519 [12] Nikolopoulou E, Eikenberry SE, Gevertz JL, Kuang Y. 2017 Mathematical modeling of an  
520 immune checkpoint inhibitor and its synergy with an immunostimulant. DCSB-B **22**, 11.  
521 (doi:10.3934/dcdsb.2020138).
- 522 [13] Lai X, Friedman A. 2017 Combination therapy of cancer with cancer vaccine and immune  
523 checkpoint inhibitors: A mathematical model. PLoS ONE **12**, 5, e0178479.
- 524 [14] Zhao B, Zhang C, Forsten-Williams K, Zhang J, Fannon M. 2010 Endothelial cell capture of  
525 heparin-binding growth factors under flow. PLoS Comput Biol **6**, 10, e1000971.
- 526 [15] Olwin B, Hauschka S. 1988 Cell surface fibroblast growth factor and epidermal growth factor  
527 receptors are permanently lost during skeletal muscle terminal differentiation in culture. J Cell  
528 Biol **107**, 761–769.

- 529 [16] Nikolopoulou E, Johnson L, Harris D, Nagy J, Stites E, Kuang Y. 2018 Tumour-immune  
530 dynamics with an immune checkpoint inhibitor. Letters in Biomathematics **5**, supl1, S137–  
531 S159. (doi:DOI:10.1080/23737867.2018.1440978).
- 532 [17] Grünewald S, Politz O, Bender S, Hérault M, Lustig K, et al UT. 2019 Rogaratinib: A potent  
533 and selective pan-fgfr inhibitor with broad antitumor activity in fgfr-overexpressing preclinical  
534 cancer models. Int J Cancer **45**, 5, 1346–1357.
- 535 [18] Schuler M, Cho B, Sayehli C, Navarro A, Soo R, et al HR. 2019 Rogaratinib in patients with ad-  
536 vanced cancers selected by fgfr mrna expression: a phase 1 dose-escalation and dose-expansion  
537 study. The Lancet Oncology **20**, 10, 1454–1466. (doi:10.1016/S1470-2045(19)30412-7).
- 538 [19] Collin MP, Lobell M, Hübsch W, Brohm D, Schirok H, Jautelat R, Lustig K, Bömer U,  
539 Vöhringer V, Hérault M, et al. 2018 Discovery of rogaratinib (bay 1163877): a pan-fgfr in-  
540 hibitor. ChemMedChem **13**, 5, 437–445.
- 541 [20] Cariboni J, Gatelli D, Liska R, Saltelli A. 2007 The role of sensitivity analysis in ecological  
542 modelling. Ecological Modelling **203**, 1-2, 167–182.
- 543 [21] Blower SM, Dowlatabadi H. 1994 Sensitivity and uncertainty analysis of complex models of  
544 disease transmission: an hiv model, as an example. Int Stat Rev **62**, 2, 229–243,.
- 545 [22] Marino S, Hogue IB, Ray CJ, Kirschner DE. 2008 A methodology for performing global uncer-  
546 tainty and sensitivity analysis in systems biology. J Theoret Biol **254**, 1, 178–196.
- 547 [23] Eisenburg M, Jain H. 2017 A confidence building exercise in data and identifiability: Modeling  
548 cancer chemotherapy as a case study. J Theor Biol **431**, 63–78.
- 549 [24] Gabor A, Villaverde A, Banga J. 2017 Parameter identifiability analysis and visualization in  
550 large-scale kinetic models of biosystems. BMC Sys Biol **11**. (doi:10.1186/s12918-017-0428-y).
- 551 [25] Gallaher J, Larripa K, Renardy M, Shtylla B, Tania N, White D, Wood K, Zhu L, Passey C,  
552 Robbins M, et al. 2018 Methods for determining key components in a mathematical model

- 553 for tumor-immune dynamics in multiple myeloma. J Theoret Biol **458**, 31–46. (doi:<https://doi.org/10.1016/j.jtbi.2018.08.037>).
- 554
- 555 [26] Meshkat N, z Kuo CE C, III JD. 2014 On finding and using identifiable parameter combinations  
556 in nonlinear dynamic systems biology models and combos: A novel web implementation. PLoS  
557 ONE **9**, 10, e110261,.
- 558 [27] Chis OT, Banga J, Balsa-Canto E. 2011 Structural identifiability of systems biology models: a  
559 critical comparison of methods,. PLoS ONE **6**, 11, e27755.
- 560 [28] Raue A, Kreutz C, Maiwald T, Bachmann J, Schilling M, Klingmüller U, Timmer J. 2009  
561 Structural and practical identifiability analysis of partially observed dynamical models by ex-  
562 ploiting the profile likelihood. Bioinformatics **25**, 25, 1923–1929.
- 563 [29] Goel M, Khanna P, Kishore J. 2010 Understanding survival analysis: Kaplan-meier estimate.  
564 Int J Ayurveda Res **1**, 4, 274–278.
- 565 [30] Dovedi S, Davies B. 2009 Emerging targeted therapies for bladder cancer: a disease waiting for  
566 a drug. Cancer Metastasis Rev **28**, 3-4, 355–367.
- 567 [31] Stenehjem D, Tran D, Nkrumah M, Gupta S. 2018 Pd1/pd11 inhibitors for the treatment of  
568 advanced urothelial bladder cancer. Onco Targets Ther **11**, 5973–5989.
- 569 [32] Fassan M, Trabulsi E, Gomella L, Baffa R. 2007 Targeted therapies in the management of  
570 metastatic bladder cancer. Biologics **1**, 4, 333–406.